nature communications

Article

https://doi.org/10.1038/s41467-026-76976-5

Acoustic cell patterning reveals geometry- and substrate-dependent vasculogenesis and human embryo model development

Received: 20 June 2025

Accepted: 11 August 2026

Published online: 21 August 2026

Check for updates

Zhaoyi Xu[1,6], Weiping Li[2,3,6], Xufeng Xue[1,5], Nicholas G. Schott[2], Chenjun Shi[3], Ruxin Yang[1], Shiyu Sun[1], Jeyoon Bok[1], Jitao Zhang[3], Jan P. Stegemann[2], Jianping Fu[1,2,4] ✉ & Cheri X. Deng[1,2,3] ✉

Precise spatial organization of cells is critical for engineering functional tissues and constructing human developmental models. Here, we report the development of acoustic cell patterning (ACP), an ultrasound-based method capable of rapidly generating spatial patterns of multiple cell types on both rigid and compliant substrates without requiring chemical or physical modification of the substrates. Spatially controlled co-patterning of human endothelial and stromal fibroblast cells through ACP reveals geometry- and substrate-dependent vascular morphogenesis. Applied to human pluripotent stem cells (hPSCs) within a microfluidic device, ACP forms neural tube-like structures exhibiting in vivo-like spatially patterned gene expression, including caudal emergence of HOXC10. ACP also generates a uniform array of hPSC clusters on soft substrates, forming epiblast-like tissues that undergo spontaneous BMP-dependent amniogenesis and primordial germ cell-like specification. These in vivo-like developmental features are not observed in structures derived from patterned hPSCs using microcontact printing on stiff substrates. Together, these results demonstrate the unique capabilities of ACP for engineering spatially organized multicellular systems and modeling early human development under conditions that better mimic in vivo environments.

Spatial organization of cells, in concert with microenvironmental cues, is a central determinant of cellular behaviors, governing processes such as cell migration, differentiation, tissue patterning, and disease progression[1]. Controlling cell spatial arrangement is thus essential for engineering functional tissues and constructing in vitro models of human development for scientific discoveries and translational applications. Among existing cell patterning techniques, microcontact printing (μCP) is widely used to generate reproducible patterning by pre-coating adhesive molecules to anchor cells on stiff surfaces such as glass or poly-dimethylsiloxane (PDMS) substrates[2–4]. While capable of generating colonies with well-defined geometries and cell density, μCP constrains tissue expansion, introduces contamination risk during pre-coating of substrate [5], alters cell behavior via adhesion[6], and is incompatible with soft, more in vivo-like extracellular matrix (ECM)-based substrates. Recently, 3D bioprinting has gained substantial interest in achieving spatial control in building tissue constructs[7–9]. However, the physical demands of extrusion in 3D printing, including temperature, pressure, and cross-linking process, can impair cell

[1]Department of Mechanical Engineering, University of Michigan, Ann Arbor, MI, USA. [2]Department of Biomedical Engineering, University of Michigan, Ann Arbor, MI, USA. [3]Department of Biomedical Engineering, Michigan State University, East Lansing, MI, USA. [4]Department of Cell & Developmental Biology, University of Michigan Medical School, Ann Arbor, MI, USA. [5]Present address: Division of Developmental Biology, Center for Stem Cell and Organoid Medicine, Cincinnati Children's Hospital Medical Center, Cincinnati, OH, USA. [6]These authors contributed equally: Zhaoyi Xu, Weiping Li.
✉e-mail: jpfu@umich.edu; dengche6@msu.edu

viability[9–11], making it challenging to construct tissue models from cells such as human pluripotent stem cells (hPSCs) that are sensitive to culture conditions. These difficulties hinder the development of in vitro models that require patterned multicellular structures sensitive to the cell microenvironment.

Leveraging the developmental potential of hPSCs[12,13], in vitro human embryo models derived from hPSCs that mimic early embryogenic events[14–20] provide essential tools to interrogate early human development, disease mechanisms, and drug responses[2,21–29]. These models overcome the ethical and technical limitations in assessing native embryonic tissues and the inability of animal models to recapitulate human-specific developmental features. hPSCs undergo morphogenetic self-organization under suitable culture conditions and can form multicellular structures with molecular, cellular, and architectural features resembling early embryonic tissues[2,21,23,24,27,29]. However, protocols of human embryo modeling typically rely on stochastic aggregation of disassociated hPSCs, often with heterogeneous cell distribution, inconsistent morphologies, and low efficiency[14–16,19,30]. For instance, neural tissues derived from spontaneous differentiating hPSCs in conventional 3D cultures frequently lack the spatial organization characteristics of early neurodevelopment[31]. Conventional 3D cultures to form epiblast-like tissues through stochastic clustering of hPSCs often lead to heterogeneous development of these structures[17,18].

These challenges motivate this study to develop acoustic cell patterning (ACP) for controlling spatial organization of cells to improve tissue organization of multicellular systems and hPSC-derived embryo models[2,3,32]. ACP employs plane-traveling ultrasound waves to rapidly organize free-floating cells into spatial patterns. Without requiring chemical or structural substrate modification or the need for creating pre-defined adhesive regions, ACP allows for contactless, free-form cell patterning, capable of generating multicellular structures on both hard and compliant substrates, including tissue culture plates, hydrogels, and within microfluidic platforms.

A variety of both labeling-based and label-free patterning technologies have been developed to achieve spatial cell patterning, advancing the engineering of complex tissue architectures and embryonic models. For example, Sloan et al. used a magnetic approach to assemble organoids into assembloids[33]. Within the field of acoustic manipulation, acoustic radiation force (ARF) has emerged as a powerful and non-invasive tool for directing cellular organization. Early efforts utilized short-path-length ultrasound standing-wave traps to investigate the physical environment of 2D cell aggregates[34]. Since then, ultrasound standing waves have been successfully used to promote cellular organization: Hocking and colleagues employed standing-wave fields to create vascular networks within 3D hydrogels[35,36] and to study ultrasound-driven vascular morphogenesis[37]. Recent advancements have further expanded the capabilities of ultrasound-based techniques, enabling the assembly of multilayered, brain-like constructs[38] and the engineering of anisotropic muscle tissues[39]. Notably, high-resolution acoustic patterning has been used to quantify spatiotemporal cell organization via Voronoi tessellation[40] and to construct functional collateral cylindroids for therapeutic applications[41]. Most recently, Armstrong et al. demonstrated high-resolution cell patterning to engineer cartilage constructs in agarose[42], while others have generated multicellular patterns[43].

However, these traditional acoustic approaches often depend on fixed standing-wave geometries, which require parallel reflective surfaces or specific spatial arrangements of transducers tuned to particular wavelengths to achieve cell aggregation. These constraints can limit the compatibility and adaptability of such systems with standard laboratory equipment and cell culture systems. In contrast, ACP employs a plane, traveling ultrasound wave generated by a single transducer that transmits through a customizable, 3D-printed thin-plate structure placed beneath a standard glass-bottom tissue culture dish. This setup generates a structured ARF field within the dish to drive cell patterning, eliminating the need for specialized reflective housing or special modifications to the cell culture dish. The ACP configuration offers a a small footprint with high flexibility, conveniently built on off-the-shelf transducers and easy swapping of plate geometries for multi-step or multi-cell type patterning in standard tissue culture plates or even microfluidic devices.

In this work, we show geometry- and substrate-dependent vascular morphogenesis and vasculogenesis generated using ACP from controlled, co-patterned human endothelial and stromal fibroblast cells as well as key embryonic developmental events in hPSC-derived embryo models, features absent or not possible with μCP on stiff substrates. Integrated with a microfluidic device, ACP generates neural tube-like structures (NTLS) with rostral-caudal (R-C) patterning. ACP also generates a uniform array of hPSC clusters on compliant ECM beds, forming epiblast-like cysts that exhibit inward embedding into the underlying matrix and spontaneous BMP-dependent amniogenesis and germline cell specification, key peri-implantation human developmental milestones that are not recapitulated in hPSC cysts generated on solid substrates.

Results

ACP achieves free-form cell patterning

In ACP, an ultrasound wave is applied to propagate through a 3D-printed thin plate placed underneath a standard glass-bottom culture dish to rapidly pattern cells without direct physical contact (Fig. 1a). Within seconds of ultrasound application, randomly distributed cells in suspension in the dish are rapidly organized into parallel lines or bands (Fig. 1b) or other two-dimensional (2D) configurations (Fig. 1c), depending on the design of the thin plate (Figure S1 and Figure S2). For example, using a plate with a 2D array of circular holes (Figure S2a), ACP generates a distinct secondary acoustic pressure field (Figure S2b, c), producing a spatially modulated ARF field that organizes normal human lung fibroblasts (NHLFs) into a spatial pattern matching the hole-array plate (Figure S2d).

Finite element analysis (FEA) simulations using a COMSOL model (Supplementary Code 1) show that the incident ultrasound wave transmitting through a slit structure excites an anti-symmetric Lamb wave within the glass substrate (Figure S1a, b). This, in turn, generates a secondary acoustic pressure field in the culture medium inside the dish, characterized by periodic pressure maxima in x-direction that is orthogonal to the orientation of the slits (Fig. 1d and Figure S1c). The gradients of the secondary acoustic pressure field establish an ARF field via momentum transfer[44,45] on suspended cells in a location-dependent manner (Fig. 1e and Figure S1d), driving them toward local force minima where stable cell patterns emerge.

FEA simulations further reveal a resonant phenomenon of the secondary acoustic pressure field, depending on the frequency of the incident ultrasound wave and the geometric dimensions of the slit structure (Fig. 1f, g). Under a resonant condition with a slit period of 0.8 mm, slit width of 0.4 mm, acoustic pressure of 0.1 MPa, and frequency of 1.68 MHz (condition A in Fig. 1f), the ARF acting on a 10 μm-radius cell reaches ~0.4 nN in the x-direction and ~0.2 nN in the z-direction (Fig. 1h). Under another resonant condition (condition B in Fig. 1g; slit period: 1.8 mm; width: 0.8 mm; frequency: 0.56 MHz), the ARF magnitude is substantially lower (Fig. 1h), resulting in broader line widths of patterned cells. Larger inter-line spacing is also generated in condition B, compared to under condition A, corresponding to the greater spacing between the slits (Fig. 1i). These results confirm that the spatial and amplitude characteristics of ARF determine spatial cell patterning in ACP. In practice, the efficiency and fidelity of cell patterning are also impacted by ACP application duration and the property of culture medium surrounding the cells. For instance, a 0.2 nN ARF is sufficient to displace a cell by 200 μm within ~ 0.13 s in cell culture medium, which has a viscosity comparable to that of water

https://doi.org/10.1038/s41467-026-76976-5

(~0.0007 Pa·s), whereas this time increases to ~2.64 s when medium viscosity becomes 20 times greater. Thus, for cells suspended in culture medium, which has a relatively low viscosity, ACP achieves spatial organization of cells quickly in the order of seconds, forming stable cell pattern after cells attach to the substrate, typically within 30 min after ACP application.

To pattern cells in biologically relevant hydrogels, ACP is applied to spatially organize cells before hydrogel gelation, forming a stable cell pattern in a solidified hydrogel. Geltrex, a basement membrane matrix widely used to support mammalian cell adhesion, proliferation, and differentiation[19,30], remains liquid at 4 °C and undergoes gelation above 15 °C within 5–10 min. Applying ACP using a slit structure for 10 s to hPSCs suspended in 30% liquid Geltrex maintained at 4 °C generates a line pattern of hPSCs, which become immobilized as Geltrex transitions from liquid to gel as it warms up to room temperature.

The cell density and width of the line patterns of hPSCs generated in Geltrex using ACP depend on acoustic pressure of the incident ultrasound wave (Fig. 1j) and initial cell seeding density (Fig. 1k). At a constant seeding density of 10×10^6 cells/mL, increasing acoustic pressure from 0.075 MPa to 0.24 MPa leads to increased cell density within lines (from 1.5×10^3 to 3.5×10^3 cells/mm^2) and decreased line width (from 150.4 ± 8.1 μm to 91.2 ± 5.4 μm) (Fig. 1j). Under a constant acoustic pressure of 0.15 MPa, increasing the seeding density from 5×10^6 to 40×10^6 cells / mL results in increased cell density (from 3×10^3 to 5×10^3 cells/mm^2) and line width (from 69.3 ± 5.7 to 146.4 ± 6.5 μm) (Fig. 1k). Since ACP employs ultrasound waves of low intensity, it generates minimal temperature increases that are less than 1.5 °C (Figure S3), and hPSCs maintain high viability after ACP exposures as shown by flow cytometry assay (Figures S4–S11).

These results show that ACP achieves spatial organization of cells in a standard cell culture dish without the need for structural or chemical modification of the substrate. Unlike μCP, ACP captures nearly all initially dispersed cells in culture medium into spatial patterns, thereby minimizing cell loss as no post-patterning washing steps are needed. This feature provides useful advantages when working with low-abundant cell populations or cells with high sensitivity to multi-step handling.

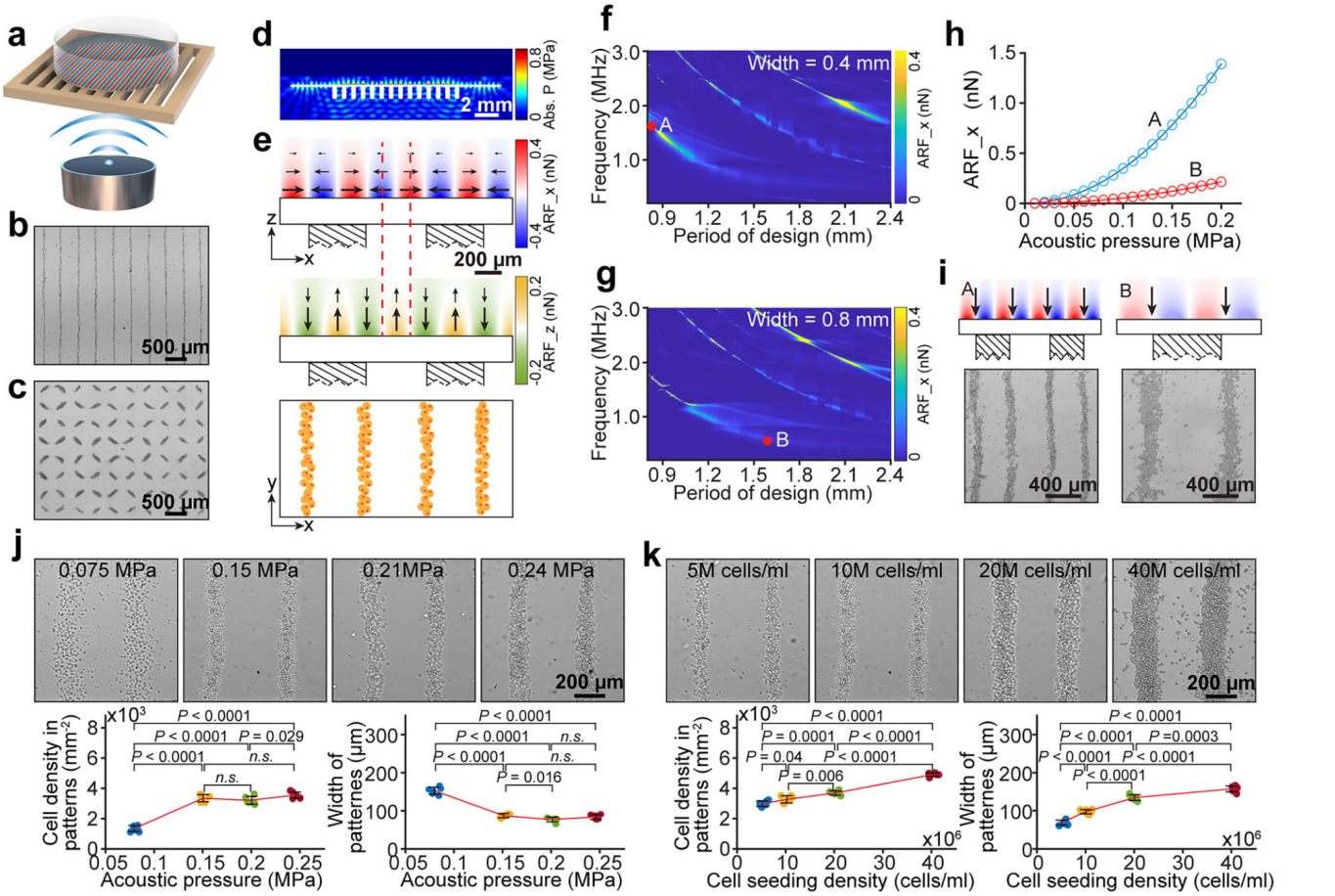


Fig. 1 | Acoustic cell patterning (ACP) platform and characterization of the acoustic radiation force field. a ACP uses an ultrasound wave traveling through a 3D-printed plate structure placed underneath a glass-bottom cell culture dish for spatial organization of cells. **b**, **c** Examples show a line pattern and a 2D pattern of normal human lung fibroblasts (NHLFs) respectively generated using ACP. Ultrasound wave application was 10 s at 1.68 MHz and 0.1 MPa. **d** Global view of the simulated acoustic pressure field generated in ACP using a slit structure placed underneath a glass-bottom cell culture dish. **e** Normalized acoustic radiation force (ARF) field in *x*-*z* plane (top) and *x*-*y* plane (middle) inside the dish generated by ACP as well as a schematic of the patterned cells (bottom). The slit structure is placed in *x*-*y* plane with slits in *y*-direction. **f** Normalized ARF in *x*-direction vs. frequency of incident ultrasound wave and the period of slit structure. Slit width is 0.4 mm. **g** Normalized ARF in *x*-direction vs. frequency of incident ultrasound wave and period of slit structure. Slit width is 0.8 mm. **h** ARF in *x*-direction as a function of the acoustic pressure amplitude of the incident ultrasound wave generated in ACP using parameters at point **A** in (**f**) and point **B** in (**g**). **i** Normalized ARF field in *x*-*z* plane and the resulting line pattern of cells generated using parameters at **A** in (**f**) (left) and parameters at **B** in (**g**) (right), respectively. **j** Representative bright field images of line patterns of hPSCs generated using ACP (top), cell density within the patterned lines (bottom, left), and line width (bottom right) vs. acoustic pressure of the incident ultrasound wave, respectively. Cell seeding density 10 M cells/mL. Data are presented as mean ± s.d. $n = 3$ independent experiments. **k** Representative bright-field images of line patterns of cells formed using ACP (top), cell density within the patterned lines (bottom, left), and line width (bottom, right) vs. cell seeding density, respectively. Data are presented as mean ± s.d. The acoustic pressure of the incident ultrasound wave is 0.15 MPa. $n = 3$ independent experiments. Source data are provided as a Source Data file.

ACP enables spatial patterning of single and multiple cell types

ACP can organize cells into spatial patterns through sequential patterning steps using the same plate structure or by employing plate structures with different geometries or dimensions (Figure S12). For example, an ACP application for 10 s with a slit plate aligns NHLFs into a line pattern. After allowing the cells to attach to the glass coverslip for 30 min, a second population of NHLFs is introduced, followed by another 10-s ACP application with the same slit structure shifted parallelly by 50 μm. This multi-step ACP patterning produces an interleaved parallel line pattern composed of the two cell populations (Figure S12a). If the second ACP is applied with the slit structure rotated by 90°, an orthogonal grid pattern composed of the two cell populations is generated (Figure S12a).

Interestingly. if the sequential orthogonal patterning is done without allowing cells to attach after the first ACP application, a regular array of cell clusters can be generated instead, as shown in the example in Figure S12b. Here, after an initial ACP application that forms lines of NHLFs, a second ACP is immediately applied to the aligned but not yet unattached cells with the slit structure rotated by 90°, the cells in the lines are then driven into discrete positions along the orthogonal direction, producing a regular array of cell clusters (Figure S12b).

ACP generates lumenized endothelial structures

The capability of ACP in generating spatially controlled cell patterning is exploited to influence vascular morphogenesis by controlling the spatial organization of human umbilical vein endothelial cells (HUVECs), either alone or with NHLFs under various conditions (Fig. 2 and Figure S13). Here, NHLFs, as stromal support cells, secrete ECM and paracrine signals to support HUVEC survival and stabilize nascent vasculature[46]. In these experiments, ACP (duration 10 sec, 0.12 MPa, 1.68 MHz; slit period: 0.8 mm; width: 0.4 mm) is applied to cells suspended in fibrinogen solution, which solidifies with the addition of thrombin right before ACP exposure. Co-patterning of HUVECs and NHLFs (cell ratio of 1:1) across varying seeding densities reveals striking differences in vascular network morphology after five days of co-culture (Figure S13a). As shown by quantitative image analysis using 2D fast Fourier transform (FFT)[47], co-patterning of HUVECs and NHLFs by ACP results in an eight-fold increase in the alignment of angiogenic sprouts compared to those from a randomly seeded mixture of HUVECs and NHLFs (Figure S13b, c). Enhanced network connectivity, indicated by the increased total sprout length within a defined region of interest and the average length of individual sprouts, particularly at higher seeding densities, is also observed for ACP-enabled co-patterning of HUVECs and NHLFs (Figure S13e). Moreover, the number of branching points remains relatively constant, suggesting that ACP primarily enhances vascular elongation and alignment rather than branching complexity (Figure S13e). These results generated via ACP applications for 10 – 20 sec are consistent with commonly observed vasculogenesis from HUVECs.

ACP is also applied to enable vascular assembly from spatially controlled, co-patterning of HUVECs and NHLFs on both rigid (glass) and compliant (fibrin gel) substrates (Fig. 2). Red and green dye-labeled NHLFs are used to show their spatial patterning on glass (Fig. 2a) or on top of a soft fibrin hydrogel (Fig. 2b) with or without physical separation between the two cell populations. By day 7, vessel-like structures with narrow lumens are formed from HUVECs co-patterned with NHLFs on glass (Fig. 2c). In contrast, when patterned HUVECs are spatially separated from NHLFs, either on glass (Fig. 2d) or atop a soft fibrin gel (Fig. 2e), they form significantly larger and more defined lumens (Fig. 2f), as shown by an increased lumenal cross-sectional area, from $3.1 \pm 3.9\ \mu m^2$ (direct co-patterning on glass) to $335.9 \pm 85.4\ \mu m^2$ (on glass with spatial separation) and further to $885.1 \pm 187.0\ \mu m^2$ (on soft gel with spatial separation). These data suggest the effects of spatial organization of HUVECs in relation to NHLFs as well as the surrounding ECM on vasculogenesis. The capability of ACP for achieving multicellular patterning could be useful for improving in vitro vascularized tissue models[48,49] by controlling cell-cell interaction.

ACP enables construction of neural tube-like structures (NTLS)

Similar to patterned hPSC colonies generated by μCP for neural induction and regional patterning in a microfluidic gradient environment[50], ACP is applied to hPSCs suspended in 30% Geltrex at low temperature (on ice) to rapidly form line patterns in a glass-bottom microfluidic device within 10 s (Figure S14 and Fig. 3a). The patterned hPSCs in Geltrex start to self-organize within 24 h (Supplementary Movie 1). By day 3, they form discernible apical lumens, similar to those formed by μCP-patterned hPSC colonies (Fig. 3a).

To achieve controlled morphogen gradients along the length of ACP-patterned hPSC colonies, the microfluidic device is designed with five channels separated by four rows of microposts (Fig. 3a). With a diameter of 200 μm and spaced 150 μm apart from each other, the microposts compartmentalize different fluid phases, *i.e.*, sequentially loaded cell-laden liquid Geltrex, acellular liquid Geltrex, and culture medium within the central channel, Geltrex channel, and two medium channels, respectively (Fig. 3b).

Following initial generation of patterned hPSCs using ACP, gradients of CHIR99021, FGF8, and retinoic acid (RA) are applied through the medium channels of the microfluidic device to establish morphogen gradient along the length of hPSC colonies (the rostral-caudal or R-C axis) between days 2 and 5, in addition to basal neural induction medium (NIM) applied uniformly in the central channel (Fig. 3b). CHIR99021, FGF8, and RA are selected for their well-established roles in axial neural patterning: CHIR99021 activates WNT signaling to promote caudal neural identity[51,52], FGF8 supports posteriorization and midbrain-hindbrain boundary formation[53,54], and RA functions as a morphogen that regulates HOX gene expression in a concentration-dependent manner[55,56]. Together, these gradients recapitulate the combinatorial signaling environment that drives spatially patterned NT development in vivo.

The patterned hPSC colonies generated using both ACP and μCP platforms are structurally similar on day 4 as elongated tubular structures, and they both express neural progenitor marker SOX2 and exhibit lumenal localization of Ezrin and ZO-1 and membrane-associated expression of β-catenin (Figure S15).

By day 7, ACP-patterned hPSC colonies form NTLS that display spatially ordered expression domains of HOXB1, HOXB4, and HOXC9 along the R-C axis. OTX2, a transcription factor specifying anterior neural fates (forebrain and midbrain), is detected at the rostral end of NTLS anterior to the HOX-positive regions (Fig. 3b), supporting faithful R-C neural patterning. While HOXC9 is localized to the caudal NTLS region by day 7, HOXC10 expression is absent at this stage (Fig. 3b).

Notably, extending the culture of ACP-patterned NTLS under continuous morphogen gradients until day 14 results in the emergence of a HOXC10-expressing domain at the distal caudal end (Fig. 3c). At this stage, the rostral and caudal ends of ACP-patterned NTLS exhibit significant tissue growth, extending out of the central channel through the spaces between adjacent posts (Fig. 3c). This outward growth demonstrates that ACP-patterned NTLS possesses the capacity for axial extension beyond its intial pattern. In contrast, NTLS formed by μCP remains morphologically constrained without the caudal emergence of the HOXC10 expression domain (Fig. 3d). In these cases, the cells are anchored directly to the pre-patterned 2D surface.

ACP-generated NTLS exhibit caudal fate independent of proliferation and tubule length

To investigate whether more caudal fates, specifically expression of HOXC10, emerge exclusively in ACP-generated NTLS and not in μCP-patterned ones due to differences in proliferation or tissue elongation,

https://doi.org/10.1038/s41467-026-76976-5

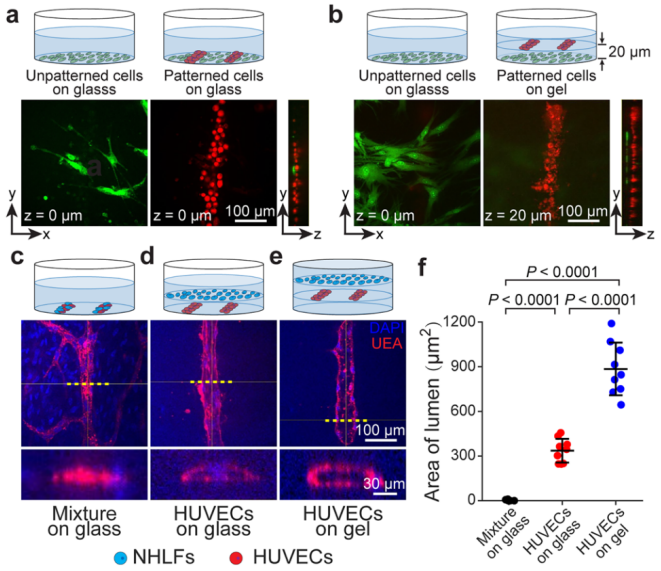


Fig. 2 | Multilayered and 3D co-patterning of cells and engineered vascular lumen formation using ACP. a ACP application to pattern NHLFs (stained in red) on top of an underlayer of unpatterned NHLFs (stained in green) seeded on the glass bottom of a cell culture dish; colors reveal the spatial relationship of the cells. **b** ACP application to pattern NHLFs (red) on top of a solidified fibrin gel layered over unpatterned NHLFs (green) on the glass well bottom; colors reveal the spatial relationship of the cells. **c**–**e** ACP applied to HUVECs to promote tube formation over 7 days in culture, with representative confocal images from above and cross-section at the dotted line, respectively, showing HUVECs patterned directly on a layer of unpatterned NHLFs (**c**), HUVECs patterned on glass and covered by a layer of fibrin and unpatterned NHLFs (**d**), as well as HUVECs patterned on a layer of fibrin gel and covered by an additional layer of fibrin and unpatterned NHLFs (**e**). **f** Areas of the lumen for those in (**c**–**e**), respectively. ACP was applied for 10 s using ultrasound waves at 1.68 MHz and 0.15 MPa. Slit structure: period 0.8 mm and slit width 0.4 mm. Data are presented as mean ± s.d. Cell seeding density was 1 M cells/ml. $n = 3$ independent experiments. Source data are provided as a Source Data file.

EdU assay is performed on both NTLS generated using ACP and μCP and our EdU assay data show similar proliferative profiles: uniformly distributed proliferating cells on day 3 (Figure S16a, c), followed by a shift of proliferating cells toward the rostral end by Day 5 (Figure S16b, d). Increasing the adhesive pattern length in μCP (from 4 mm to 6 mm) does not induce caudal HOXC10 expression (Figure S17), whereas shortening the initial ACP-patterned NTLS length from 4 mm to 2 mm still results in robust HOXC10 expression by Day 14 (Figure S18).

Examination of the mechanotransductive signaling in μCP- and ACP-patterned NTLS through immunostaining of YAP revealed that on day 1, a lower percentage of cells with nuclear YAP is seen in μCP-generated structures than in ACP-patterned tissues (Figure S19). This difference might be associated with a difference in cell anchorage.

Together, these results indicate that caudal emergence of HOXC10 in ACP-generated NTLS but not in μCP-patterned ones is not attributed to differences in proliferation or tissue length in these two systems. Rather, axial elongation of NTLS, which is promoted by a relatively unconstrained 3D environment in ACP, might be a determinant factor of caudal emergence of HOXC10 expression in NTLS during its progressive R-C neural patterning[57]. Morphogenetic changes in tissues are tightly connected with gene expression patterns: gene expression controls cell behaviors that drive tissue shape changes, while tissue morphogenesis influences gene expression through mechanical and spatial cues. This dynamic feedback loop ensures robust, self-organizing development, with both processes constantly shaping each other. Thus, ACP might offer a more flexible cell patterning tool for modeling developmental processes than traditional surface-patterning methods by better mimicking the unconstrained, 3D morphogenetic in vivo environment.

We also used the microfluidic platform to establish antiparallel morphogen gradients along the length of ACP-patterned NTLS to model dorsoventral (D-V) neural patterning (Figure S20a). Opposing gradients of *BMP4*, RA, and smoothened agonist (SAG, a sonic hedgehog or SHH signaling agonist) are introduced to recapitulate the in vivo D-V patterning signal environment[58]. *BMP4* directs neural crest specification and dorsal neural patterning[59], SHH (mimicked by SAG) serves as a key ventralizing cue secreted from the notochord and floor plate, and RA modulates neural progenitor identity while enhancing cellular responsiveness to both BMP and SHH signaling[60,61]. This combinatorial gradient system successfully induces spatially patterned expression of canonical D-V neural lineage markers, with *SOX10* and *PAX3* expressed dorsally and *OLIG2* confined to ventral domains (Figure S20b).

There are two advantages for choosing the long axis (length direction) of ACP-patterned NTLS as its D-V axis for demonstrating D-V patterning. Firstly, this allows clear detection of spatially segregated expression domains of canonical D-V neural lineage markers along the length of NTLS. Secondly, this strategy is compatible with the design of the microfluidic gradient device and ACP operation to enable the scalable formation of D-V patterned NTLS in the microfluidic device. Together, our data highlight the capability of ACP to generate neural tissue models that can exhibit regional patterning along both R-C and D-V axes, respectively. Future follow-up studies are needed to develop innovative approaches to apply ACP to achieve neural patterning in the orthogonal R-C and D-V axes simultaneously in the same neural tissue.

ACP generates human epiblast models

ACP sequential cell patterning (Figure S2b) is used to generate a spatially organized array of hPSC clusters with a uniform size (Figure S14a). In ACP, the number of hPSCs in each cluster could be modulated by controlling the initial cell seeding density. As the seeding density increases from 32×10^3 to 58×10^3 cells cm^{-2}, the average number of hPSCs in each cluster increases from 22.2 ± 8.2 to 50.4 ± 12.0 (Figure. S21b, c). Upon subsequent culture, ACP-patterned hPSC clusters exhibit more notable expansion on day 3 than μCP-generated clusters, with cell number per cyst reaching 33.6 ± 14.9 as compared to 20.1 ± 15.8 in μCP-generated clusters (Figure S21d). Randomly seeded, un-patterned hPSCs, in comparison, form cell clusters with a much wider range of cell number per cluster, 36.8 ± 34.7 (Figure S21d). Compared to the cysts formed from unpatterned hPSCs (Figure S22a), ACP-generated hPSC clusters translate into more consistent 3D hPSC cysts in size and morphology on day 6 (Figure S22b).

We examined tissue morphology and marker expression related to structural organization and mechanotransductive state for hPSC clusters on glass, under ACP, μCP, and random seeding conditions. Our results (Figure S23) show that hPSC colonies from μCP show a prominent radial organization and cell-cell junctions on day 1, with a single central apical lumen, marked by *EZRIN* and ZO-1, emerging at the colony center. In contrast, on day 1, hPSC colonies from ACP and random cell seeding appear as disorganized loose cell aggregates without a central lumen. By Day 3, μCP-generated clusters have resolved into highly uniform, spherical cysts with a single, large central lumen marked by apical localization of *EZRIN* and *ZO-1*. Conversely, hPSC clusters formed by ACP and random cell seeding remain largely disorganized, often exhibiting multiple small lumens.

To leverage the capability of ACP for spatial cell patterning on soft substrates, which provide a more embryonic-like culture environment, ACP is applied to pattern hPSCs into clusters on soft Geltrex matrix (ECM) beds or glass substrates, with diluted Geltrex (4%) added to culture medium to establish a 3D environment (Fig. 4a). The hPSC clusters self-organize into epithelialized cystic structures within 4 days on both ECM bed or glass substrates, featuring a central apical lumen

https://doi.org/10.1038/s41467-026-76976-5

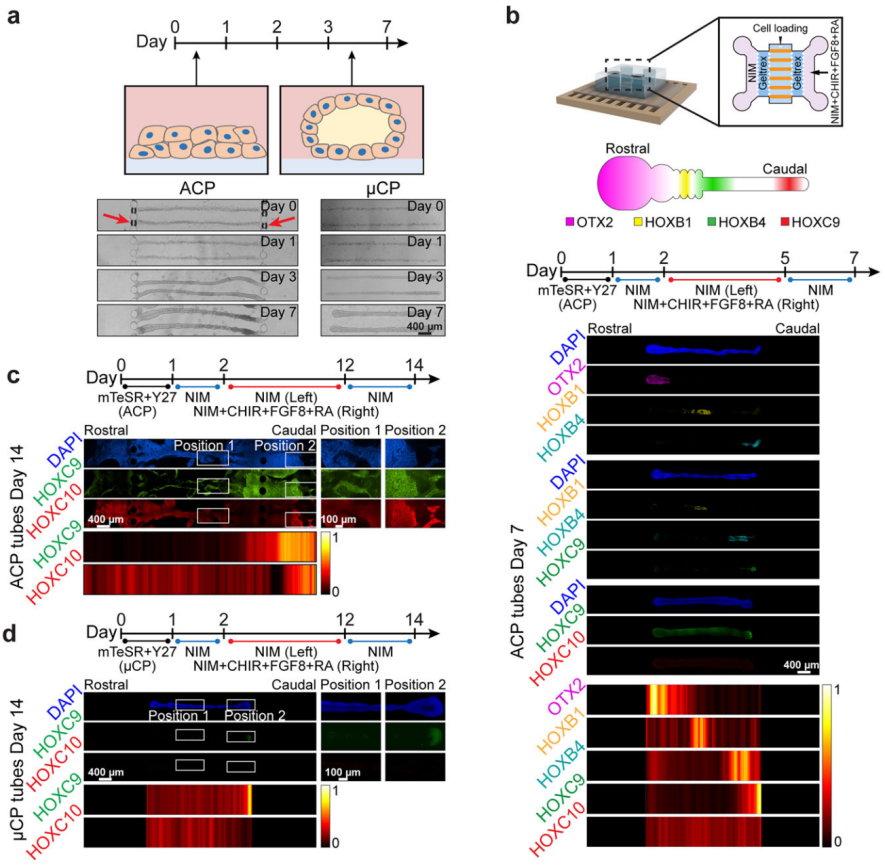


Fig. 3 | ACP-directed patterning of hPSCs establishes rostral-caudal identity in neural tube-like structures. a Patterning and culture of hPSCs in 30% Geltrex using ACP (left) and μCP (right) in a microfluidic device, respectively. Red arrows indicate the small gas packets trapped between two adjacent posts. **b** Top: Schematic diagram and protocol for patterning hPSCs using ACP inside a microfluidic device to establish a morphogen gradient along the direction of patterned stripes of hPSCs. Bottom: Immunostaining images and heatmaps ($n = 5$) showing spatially distinct appearance of HOXB1, HOXB4, HOXC9, and OTX2 in the rostral-caudal (R-C) axis of the NTLS on day 7. **c** Immunostaining images and heatmaps ($n = 4$) showing R-C patterning of NTLS generated using ACP in terms of HOXC9 and HOXC10 on day 14. **d** Immunostaining images and heatmaps ($n = 5$) of R-C patterning of NTLS generated using μCP showing HOXC9 and HOXC10 on day 14. ACP application duration 10 s, ultrasound frequency 1.68 MHz, 0.24 MPa, slit structure period 0.8 mm and width of 0.4 mm. NIM: neural induction medium. Source data are provided as a Source Data file.

marked by *EZRIN* and *ZO-1* expression, mimicking the peri-implantation stage epiblast structure (Fig. 4b and Figure. S24).

While hPSCs can self-organize and form lumenal structures regardless of whether the cells are patterned on glass surfaces or ECM beds, the hPSC cysts on ECM beds display more symmetric morphologies, quantified by width-to-height ratios, compared to those generated on glass surfaces using ACP (Fig. 4c and Figure. S25). Interestingly, ACP-generated cysts on ECM beds exhibit progressive ingrowth into the underlying Geltrex matrices (Fig. 4d, Figure S25a–c), a phenomenon not possible in those cultured on rigid glass substrates (Figure. S25d–f).

To more directly exclude potential effects of ultrasound itself on cellular state, we performed comparative experiments to compare the pluripotent markers in ACP-treated hPSCs that were subsequently cultured under random seeding conditions on a glass substrate with untreated hPSCs cultured under random seeding conditions. Our results (Figure. S26) show that the pluripotent markers remained stable; ultrasound exposure did not impact the levels of pluripotency markers in the cells.

While ACP-generated hPSC cysts formed on glass substrates retain pluripotency with high levels of expression of core pluripotency markers OCT4, NANOG, and SOX2, those formed and grown on soft Geltrex beds exhibit spontaneous differentiation with decreased expression of OCT4 and NANOG, even in the absence of exogenous differentiation factors (Fig. 5a, b). Spontaneous differentiation of hPSC cysts on soft Geltrex beds is abolished with BMP inhibitor LDN193189 added on day 2 or days 2–3 (Figure S27), supporting the involvement of BMP signaling in the observed spontaneous differentiation of hPSCs.

Quantification of expression of several *BMP* molecules (*BMP2*, *BMP4*, *BMP6*, and *BMP7*) was performed using qRT-PCR across four experimental groups: un-patterned hPSC cysts on glass (un-patterned-glass), un-patterned cysts on Geltrex beds (un-patterned-ECM), ACP-patterned cysts on glass (ACP-glass), and ACP-patterned cysts on Geltrex beds (ACP-ECM). By day 6, *BMP* expression - particularly *BMP4* - is markedly elevated in the two groups on Geltrex beds (unpatterned-ECM and ACP-ECM), with an even greater upregulation under ACP-ECM condition (Fig. 5c). No significant *BMP* expression is observed in the unpatterned-glass group, while the ACP-glass group shows moderate increases in *BMP6* and *BMP7*. At an earlier timepoint (day 4), only the ACP-ECM group exhibits elevated *BMP* expression (Figure. S28).

We further performed Brillouin microscopy to quantify the mechanical stiffness of hPSC cysts in situ formed under different conditions. Brillouin images are constructed from the Brillouin shift resulting from the interaction of incident laser light with the thermally induced acoustic phonons inherent to the material[62]. Our results show that higher levels of Brillouin shift, representing stiffer materials, are generated by ACP-patterned hPSC cysts on glass surfaces than by ACP-patterned cysts on ECM beds (Fig. 5d–f). Even greater levels of Brillouin shift are detected in μCP-generated cysts on glass substrates

https://doi.org/10.1038/s41467-026-76976-5

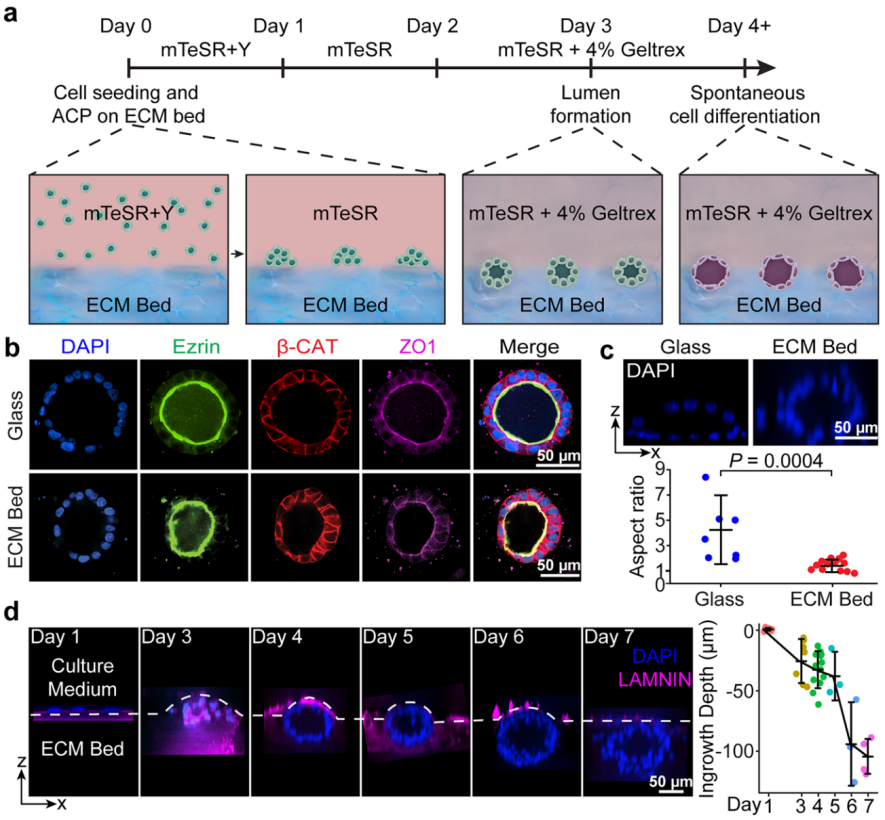


Fig. 4 | ACP enabled cyst formation on stiff and soft substrates. a Experimental protocol for generating 3D hPSC cysts. **b** Representative confocal images of ACP-generated 3D hPSC cysts on glass or ECM substrate, forming polarized single-lumen structures in 4 days, with apical membrane markers EZRIN and ZO-1, and the adherens junction marker β-catenin. Scale bar: 50 μm. Experiment was repeated independently 3 times with similar results. **c** Representative confocal z-stack images of cysts grown on glass or ECM bed on day 4 (top) and the respective aspect ratio. $n = 3$ independent experiments. Data are presented as mean ± s.d. **d** Left: Representative Z-stack confocal images of cysts on ECM bed from Day 1 to Day 7, showing cyst ingrowth into the ECM bed. Right: Quantification of cyst ingrowth. Data are presented as mean ± s.d. Cell seeding density was 45×10^3 cells cm^{-2}. $n = 3$ independent experiments. Source data are provided as a Source Data file.

(Figure S29). These data suggest the impact of both substrate stiffness and patterning method on the mechanical stiffness of hPSC cysts.

Interestingly, ACP-patterned hPSC cysts on ECM beds exhibit lower levels of Brillouin shift than ACP-generated cysts on glass surfaces at their bottom surfaces, but similar levels are detected at the middle transverse plane in both types of cysts (Fig. 5f). This suggests a greater stiffness gradient in ACP-patterned hPSC cysts on ECM beds, as compared to in ACP-generated (Fig. 5f) or μCP-generated cysts on glass (Figure S29). A similar stiffness gradient is also observed in cysts formed from randomly seeded hPSCs on an ECM bed, but not on glass substrates (Figure S29).

Amniogenesis and germline induction in ACP-generated epiblast models

Epiblast-like structures formed by hPSCs on ECM beds exhibit early hallmarks of amniotic differentiation on day 4, characterized by upregulation of GATA3, ISL1, phosphorylated SMAD1/5 (pSMAD1/5), and TFAP2A, which are known lineage markers of human amniogenesis (Fig. 6a). The proportion of cells within each cyst expressing these amniogenesis markers is significantly higher in ECM-supported cultures than in those grown on glass (Fig. 6b). In contrast, hPSC cysts cultured on glass substrates remain pluripotent without exhibiting these differentiation signatures (Fig. 6a, b). A distinct subpopulation of cells co-expressing TFAP2C, NANOG, and SOX17, markers associated with the specification of hPGCLCs, emerge in hPSC cysts on ECM beds on day 4 (Fig. 6b) and remain on day 6 (Fig. 6c). The percentage of cells per cyst with positive nuclear expression of GATA3, ISL1, pSMAD1/5, and TFAP2A respectively was significantly higher in ECM-supported cultures than in cysts on glass (Fig. 6d). Notably, the subpopulation of ECM-supported cysts that included positive specification of human primordial germ cell-like cells (hPGCLCs) increased from 34.4% (11/32) on day 4 to 45.8% (11/24) on day 6, while no hPGCLCs are detected in any of the cysts on glass on either day 4 (0/34) or day 6 (0/34) (Fig. 6e).

Amniogenesis and hPGCLC induction were also observed in hPSC cysts derived from random seeding of hPSCs on ECM beds, while no amniogenesis or hPGCLC specification was observed in hPSC cysts formed from randomly seeded or unpatterned hPSCs on glass (Figure S30). Our results reveal the emergence of a distinct subpopulation of cysts that included a significantly higher percentage of cells with decreased nuclear expression of NANO, OCT4, and SOX2 (Figure S30a). Compared to the ECM-supported cysts formed from ACP-patterned hPSCs (Fig. 6d), the cysts formed from unpatterned hPSCs produced a smaller subpopulation of cysts that included cells with positive expression of GATA3, ISL1, pSMAD1/5, and TFAP2A, respectively (Figure S30b), suggesting the patterning effects of ACP on the matched substrate condition. Similarly, compared to cysts formed from patterned hPSC using ACP (Fig. 6e), the subpopulation of ECM-supported cysts that included positive specification of hPGCLCs was much smaller, with only a few cysts with triple-positive nuclear expression of TFAP2C-NANOG-SOX17 (Figure. S30c). These data suggest the contributions of substrate stiffness and cell patterning to a lesser degree to amniogenesis and hPGCLC induction in hPSC-derived epiblast models.

Overall, these results show that on rigid glass substrates, μCP produces hPSC cysts with more regular morphology, clearer single central lumens, and tighter apical junctional organization than ACP at early time points. However, these results reveal the suitability of ACP for patterning and generating hPSC cluster arrays on soft, ECM-based

https://doi.org/10.1038/s41467-026-76976-5

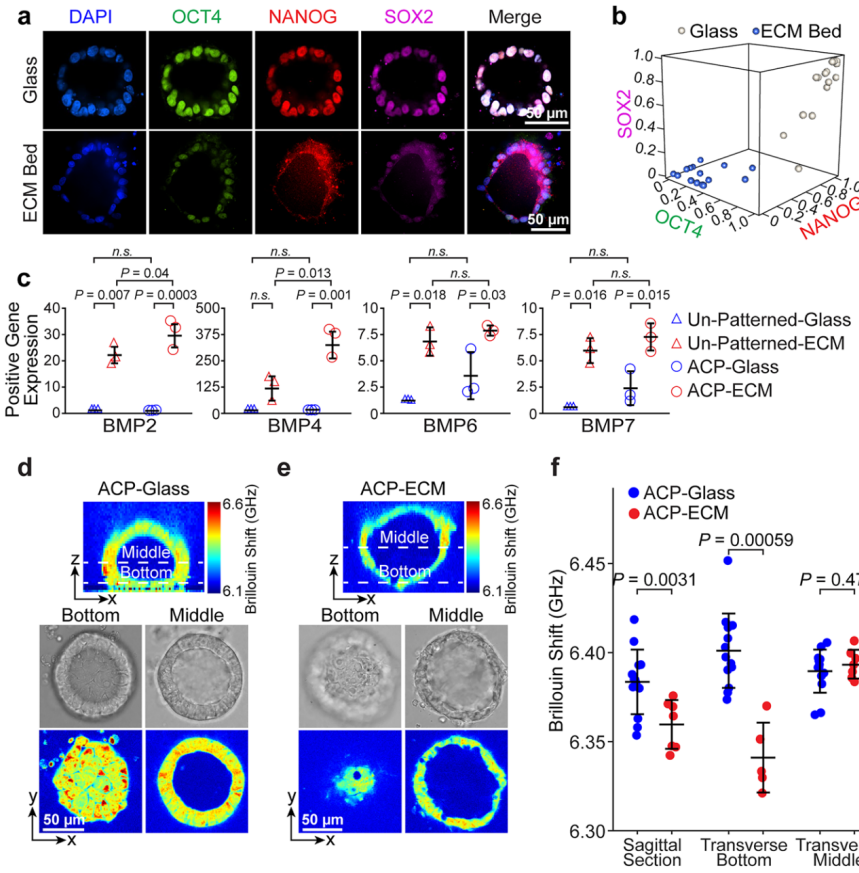


Fig. 5 | Substrate stiffness modulates the differentiation and mechanical properties of ACP-generated hPSC cysts. a Immunofluorescence staining of pluripotency markers (OCT4, NANOG, SOX2) showing differentiation of ACP-generated cysts on ECM groups and glass, respectively. The experiment was repeated independently 3 times with similar results. **b** Percentage of the cells stained positive for each immunostaining marker in cysts from ECM and glass groups on Day 4. $n = 3$ independent experiments. **c** qRT-PCR analysis of BMP pathway activity in cysts on day 6 under the four indicated conditions. Data were normalized against GAPDH and then to the glass control group. $n = 3$. Data are presented as mean ± s.d. **d, e** Brillouin-shift images of cysts formed from hPSCs patterned on glass (**d**) and ECM bed (**e**) using ACP. Top: Brillouin-shift images in *x-z* plane (sagittal plane); Lower images: the bright-field images and Brillouin-shift images in *x-y* plane (transverse plane) of the cyst near the bottom (left) and middle plane (right). **f** Brillouin shift in ACP-generated cysts on glass and ECM bed respectively. Data are presented as mean ± s.d. $n = 3$ independent experiments. Source data are provided as a Source Data file.

beds, which were more uniform compared to spontaneously formed clusters from unpatterned hPSCs on soft, ECM-based beds. This is inaccessible to μCP that requires adhesive coatings on rigid surfaces. Our observations regarding matrix ingrowth, isotropic cyst morphology, BMP-dependent spontaneous amniogenesis, and emergence of hPGCLCs are not recapitulated in cysts formed on glass, regardless of whether the underlying clusters were generated by μCP, ACP, or random seeding.

Discussion

Spatial organization of cells is fundamental to engineering complex tissue architectures and constructing faithful embryonic models for fundamental studies and translational applications. ACP is a new ultrasound-based technique that uses plane traveling ultrasound waves for rapid, free-form spatial organization of cells. The ACP method exploits the secondary acoustic pressure field generated by the forced excitation of a rigid substrate, such as a glass slide, in the form of a Lamb wave induced by an incident plane ultrasound wave. This excitation, facilitated by a 3D-printed plate structure and tuned to resonance, produces a spatially periodic ARF field with a penetration depth of approximately 100–150 μm above the substrate. The resulting ARF is sufficiently strong to enable rapid, contact-free, and efficient cell patterning without requiring chemical or structural substrate modifications. Notably, ACP captures nearly all cells in suspension, eliminating the need for surface adhesion molecules and minimizing cell loss typically associated with post-patterning washing steps. While the present work focuses on a specific slit-based plate design, the underlying principles of ACP are generalizable and can be extended to diverse plate geometries and acoustic configurations to achieve free-from-cell patterning.

The utility of ACP is explored in several use cases in this study. ACP-mediated spatial patterning of endothelial and stromal cells reveals geometry- and substrate-dependent features of vascular morphogenesis, including enhanced alignment, lumenogenesis and morphometric changes. We further demonstrate the application of ACP for multi-step and multi-cell-type patterning to control the spatial relationship of HUVECs and NHLFs, which is not readily achievable using random cell seeding or μCP.

ACP-patterned hPSCs within a microfluidic device develop into NTLS with distinctive features not observed in μCP-derived counterparts, including axial tissue elongation beyond the initial patterns as well as caudal HOX10 gene expression. These differences may be due to the less restricted tissue growth environment for ACP-patterned NTLS compared to those generated from μCP, where cells are tethered via adhesion molecules on a stiff substrate. ACP may provide a more in vivo-like cellular environment for ACP-patterned hPSC aggregates. While initial results suggest cell anchorage might impact the mechanical state and developmental trajectories of patterned tissues, the mechanistic basis of these observations remains to be elucidated using lineage tracing, live imaging, and single-cell transcriptomics

https://doi.org/10.1038/s41467-026-76976-5

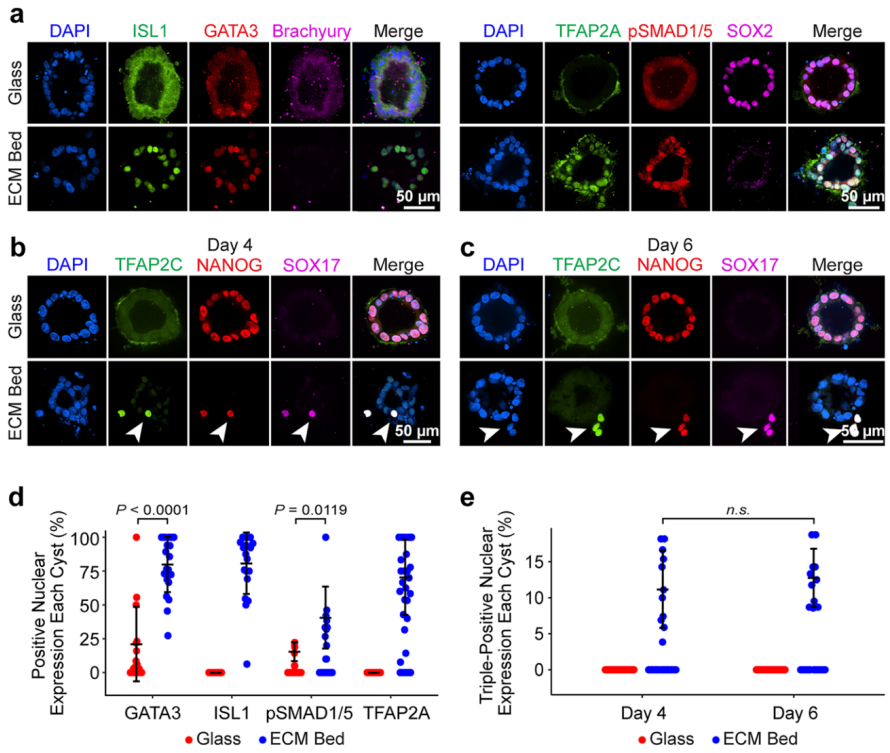


Fig. 6 | Spontaneous amniogenesis and generation of primordial germ cells (PGCs) from ACP-generated cysts on a biomimetic ECM bed. a Immunostaining images of DAPI, ISL1, GATA3, Brachyury, TFAP2A, pSMAD1/5, and SOX2 in cysts generated and cultured on glass or ECM bed on day 4, respectively. The experiment was repeated 3 independent times with similar results. **b** Immunostaining images of DAPI, TFAP2C, NANOG, and SOX17 in cysts generated on glass or ECM bed on day 4, respectively. The experiment was repeated independently 3 times with similar results. **c** Immunostaining images of DAPI, TFAP2C, NANOG, and SOX17 in cysts on glass or ECM bed on day 6, respectively. Experiment was repeated independently 3 times with similar results. **d** The percentage of cells in each cyst with positive expression of amnion markers GATA3, ISL1, pSMAD1/5, and TFAP2A on Day 4. Data are presented as mean ± s.d. $n = 3$ independent experiments. **e** The percentage of hPGCLCs with positive TFAP2C-NANOG-SOX17 co-expression in each of the cysts cultured on glass (red dots) or ECM bed (blue dots) on day 4 and day 6, respectively. $n = 3$ independent experiments. Source data are provided as a Source Data file.

technologies to dissect how morphogen gradients, ECM cues, and mechanical forces regulate NTLS morphogenesis and patterning.

ACP is capable of patterning hPSCs on soft substrates such as ECM bed, a capability not achievable using μCP. ACP generates cell clusters on soft ECM beds with a more uniform size distribution than those formed from randomly seeded hPSCs on ECM beds. The epiblast-like structures derived from ACP-patterned hPSC clusters on soft ECM substrates exhibit developmental phenotypes not observed in glass-supported cultures formed using ACP, μCP, or from randomly seeded hPSCs. These features of ACP-patterned structures on ECM beds include embedding into the supporting matrix, more isotropic cyst morphology, spontaneous amniotic differentiation, and the emergence of hPGCLCs, implicating a critical role of ECM microenvironmental cues in directing morphogenesis and lineage choices of the epiblasts during peri-implantation human development. While hPSCs possess an innate capacity for self-organization, ACP patterning promotes their structural organization and might provide additional biophysical cues to mediate intracellular mechanotransductive signaling.

Although our data suggest the involvement of BMP signaling, the relative contributions of individual BMP ligands (*e.g.*, *BMP4 vs. BMP7*) and how the ECM signals activate BMP activities, which in turn regulate lineage choices of hPSCs toward different cell fates, require additional mechanistic investigations. The specific mechanisms by which ECM properties, both biochemical composition and mechanical stiffness, influence epiblast morphogenesis and lineage diversification in ACP-patterned hPSC cysts are not fully understood. As Geltrex is an undefined, natural hydrogel (similar to Matrigel), future studies using chemically defined and mechanically tunable synthetic ECM systems are needed to isolate the effects of specific ECM parameters and improve the reproducibility and applicability of our study.

The advantages of ACP can be appreciated by a comparison with existing patterning approaches. μCP and related stencil/photolithography-based techniques offer high reproducibility and submicron resolution in terms of patterning geometry, but they fundamentally depend on pre-coated adhesion molecules on rigid substrates such as glass or PDMS. They are incompatible with soft or matrix-based substrates that better mimic the in vivo environment. In addition, these methods are not readily reconfigurable and typically require multi-step washing that leads to cell loss, a limitation particularly relevant for low-abundance or sensitive cell populations such as hPSCs. Extrusion- and inkjet-based 3D bioprinting offer programmable 3D architectures and cell-density control, but suffers from nozzle-induced shear stress that can compromise viability and function, particularly for shear-sensitive cell types such as hPSCs and neural progenitors; reported viabilities in extrusion bioprinting range from 40-90% depending on bioink rheology, nozzle geometry, and pressure, and digital light processing-based printing introduces additional concerns regarding photoinitiator toxicity and UV exposure[63]. Digital light processing-based printing achieves higher resolution but introduces photoinitiator toxicity and UV-exposure constraints. Label-based contactless approaches such as optical tweezers and dielectrophoresis offer dynamic single-cell control but typically require cell tagging, specialized electrode or laser hardware, and are not readily compatible with standard culture vessels or hydrogel-based 3D environments.

In contrast, ACP uses a single transducer and a swappable, 3D-printed thin plate placed beneath an unmodified glass-bottom dish to

generate a structured ARF field to achieve cell repositioning, eliminating the need for reflective housings used in other acoustic-based methods, surface chemistry, photoinitiators, or extrusion nozzles, with no measurable effect on viability and pluripotency with temperature increases below 1.5 °C (Figures S3–S5).

The principal limitations of ACP include a lateral resolution set by the acoustic wavelength and the geometry of the secondary pressure field (typically tens of micrometers, somewhat coarser than the few-micrometer resolution achievable by μCP), a vertical force penetration of 100 - 150 μm above the substrate that currently restricts patterning to quasi-2D or thin 3D layers rather than thick volumetric constructs, and dependence on a low-viscosity carrier for cell movements (e.g., liquid pre-gel solutions) for efficient cell repositioning. Future work that combines ACP with multi-axis transducers or layer-by-layer hydrogel deposition could extend its capability toward fully volumetric, programmable 3D constructs while preserving the substrate flexibility and cell-friendly nature that distinguish ACP from existing approaches.

In summary, results in this study show that ACP achieves rapid, free-form, contactless patterning of single or multiple cell types on both rigid (glass) and compliant (Geltrex, fibrin) substrates, and integrates seamlessly with microfluidic platforms, capabilities that are not collectively achievable with any single existing approach. ACP enables the formation of NTLS that exhibit caudal patterning of HOX genes and epiblast-like tissues on soft ECM substrates that undergo spontaneous, BMP-dependent amniogenesis and hPGCLC specification. These results, which are not observed in hPSC clusters patterned on stiff substrates using either μCP or ACP, or from randomly seeded hPSCs, demonstrate the potential of ACP for investigating how spatial patterning and microenvironmental context regulate tissue morphogenesis and cell fate decisions, with potential applications in developmental biology, tissue engineering, stem-cell research, and regenerative medicine.

Methods

This research did not involve human participants or live animals. All experiments involving human pluripotent stem cells were conducted with prior approval from the Human Pluripotent Stem Cell Research Oversight (HPSCRO) Committee at the University of Michigan, Ann Arbor (HPSCRO application #1049, approved 09 January 2023), in compliance with all relevant institutional and national guidelines. The H9 (WA09) human embryonic stem cell line was obtained from WiCell. Primary human umbilical vein endothelial cells (HUVECs) and Normal human lung fibroblast cells (NHLFs) were commercially obtained.

Cell cultures

Primary human umbilical vein endothelial cells (HUVECs) (Lonza, Walkersville, MD) were used in this study. HUVECs were plated in a tissue culture flask and grown in fully supplemented VascuLife endothelial cell culture medium (Lifeline Cell Technology, Frederick, MD). Normal human lung fibroblast cells (NHLF) were purchased (Lonza Inc., Walkersville, MD) and cultured in Dulbecco's modified Eagle medium (DMEM) supplemented with 10% FBS and 1% penicillin streptomycin. Cells were maintained at 37°C in 100% humidified air containing 5% CO2, and the medium was changed every other day. In some experiments, NHLFs were dyed red or green using CellTracker fluorescent probes (Thermo Fisher) as red or green.

Human pluripotent stem cells (hPSCs) (WA09, WiCell; NIH registration number: 0062) were used in this study. They were authenticated by original sources and in-house via immunostaining for pluripotency markers. The cells were tested negative for mycoplasma contamination (LookOut Mycoplasma PCR Detection Kit, Sigma-Aldrich). They were maintained in a standard feeder-free culture system using mTeSR1 medium (STEMCELL Technologies) and lactate dehydrogenase-elevating virus (LDEV)-free hESC-qualified reduced growth factor basement membrane matrix Geltrex (Thermo Fisher Scientific; derived from Engelbreth-Holm–Swarm tumors, similarly to Matrigel) in accordance with the manufacturer's guidelines. Cell culture was visually inspected during each passage to confirm the absence of spontaneously differentiated, mesenchymal-like cells in culture. Only hPSCs between P50 and P70 were used in this study.

Experimental setup for acoustic cell patterning (ACP)

A slit plate structure (thickness 1 mm), which includes an array of periodic, parallel slits with equal separation distance, was 3D-printed with a slit width of 0.4 mm and a period of slits of 0.8 mm, using a Formlabs 3B SLA printer with clear resin. A planar, circular ultrasound transducer (diameter 2.54 cm, center frequency 1.68 MHz; Piezo Technologies, Inc.) was used for ACP in this study and was calibrated in free field beforehand using a hydrophone (Onda, HNR-0500). The transducer, driven by an arbitrary waveform generator (33220 A; Agilent) and a power amplifier (75A250; Amplifier Research), was placed facing upward inside a small water tank, filled with deionized water for acoustic coupling. The cell culture dish or a microfluidic device housing the cells was placed above, at the Rayleigh distance of the transducer (95 mm), with only the bottom of the dish or microfluidic device submerged in water to maintain the sterility of the cells. The slit structure was placed beneath in close contact with the bottom of the cell culture dish or microfluidic device.

Theoretical framework of ACP and COMSOL simulation

In ACP, an incident planar ultrasound wave is applied to transmit through a 3D-printed plate structure placed underneath the glass slide of a glass-bottom cell culture dish, resulting in a gradient acoustic field[64–66]. The gradient pressure distribution above the glass surface originated from the interaction of the incident sound waves with the resonant excitation of a specific mode in the composite structure (3D-printed slit structure and glass plate).

The acoustic radiation force (ARF), **F**, acting on a cell in ACP is determined from the gradient of the Gor'kov potential U[67] as

$$\mathbf{F} = -\nabla U. \tag{1}$$

The Gor'kov potential is a function of the acoustic pressure (p) with the components in three directions p_x, p_y, and p_z, and is calculated using

$$U = K_1\left(|p|^2\right) - K_2\left(|p_x|^2 + \left|p_y\right|^2 + |p_z|^2\right), \tag{2}$$

where $K_1 = \frac{1}{4}V\left(\frac{1}{c_0^2\rho_0} - \frac{1}{c_c^2\rho_c}\right)$, $K_2 = \frac{3}{4}V\left(\frac{\rho_0-\rho_c}{\omega^2\rho_0(\rho_0+2\rho_c)}\right)$, which depend on the volume of the cell (V), density of the cell (ρ_c) and density of the medium (ρ_0), as well as the speed of sound in the cell (c_c) and medium (c_0), respectively.

COMSOL MULTIPHYSICS 5.4 was used to calculate the acoustic pressure distribution and ARF acting on a spherical cell using Eq. (1). The ultrasound field was modeled using the Pressure Acoustics, Frequency Domain (for water) and Structural Mechanics module (for epoxy, glass, and cell). The material parameters used in our simulation were included in Table 1.

Infrared (IR) imaging for temperature measurement during ACP application

IR imaging was used for non-destructive, non-contact temperature measurement of tissue/cell temperature in situ in this study. For measurements, an IR camera (Silver 5600, FLIR Systems, Boston, MA, USA) was positioned above and facing downward to obtain record images of the sample with and without ACP application for a total duration of 3 min at a 30 Hz frame rate. For ACP, ultrasound was

Table 1 | Material properties used in COMSOL simulation of ACP

Materials	Density (ρ)	Pressure-wave speed (c_p)	Shear-wave speed (c_s)	Speed of sound (c)
Water	1000 kg/m^3	–	–	1500 m/s
3D-printed Resin	1100 kg/m^3	2700 m/s	1600 m/s	–
Glass	2490 kg/m^3	5660 m/s	3300 m/s	–
Cell	1068 kg/m^3	1689 m/s	690 m/s	–

applied continuously for 20 s. The temperature within the region of interest as a function of time was obtained from the recorded video images.

Flow cytometry

Cells or tissues were dissociated using Accutase for 10 min at 37 °C on the day of sample collection. Cells were then washed with PBS and stained with Bioscience™ Fixable Viability Dye eFluor™ 780 (Invitrogen™) according to the manufacturer's instructions. After staining, cells were washed with PBS, resuspended in cold staining buffer, and filtered to obtain single-cell suspensions immediately prior to flow cytometric analysis.

Samples were acquired on a Bio-Rad ZE5 Cell Analyzer, with 25,000–30,000 cells recorded per group, and data were analysed using FlowJo v11. The gating strategy is shown in Supplementary Fig. S4 and gating data are available in Source Data: the primary cell population was first gated on an FSC-A versus SSC-A plot to exclude debris and non-cellular events on the basis of size and granularity, and live and dead cells were then discriminated on the basis of Fixable Viability Dye eFluor 780 signal. Unstained live cells and stained dead cells were used as compensation and gating controls. All sample groups were collected from at least three independent batches.

Patterning of HUVECs and NHLFs in a glass-bottom cell culture dish using ACP

Fibrinogen stock solutions of 4.0 mg ml^{-1} were prepared by dissolving lyophilized bovine fibrinogen (F8630, Sigma) in phosphate buffered saline (PBS; Gibco) at 37 °C. The fibrinogen solutions were filtered using a 0.2 μm PVDF syringe filter. Bovine thrombin (T6634; Sigma) was dissolved in a sterile-filtered solution of 0.1 %w/v bovine serum albumin (Sigma) in DI water to form a 50 Unit/ml stock solution.

HUVECs and NHLFs were trypsinized and suspended in DMEM at a given seeding cell density, and well mixed at a 1:1 ratio. 100 µl of 2.5 mg/ml cell-fibrinogen solution was made by mixing 62.5 µl of 4 mg/ml prepared fibrinogen, 10 µl FBS, 0.8 µl thrombin (Sigma, 50 Unit/ml) and 26.7 µl cell-DMEM.

The well-mixed cell-fibrinogen solution was quickly seeded on the glass-bottom dish (MatTek Corporation, P35G-1.5-14-C) and placed on the 3D-printed mask for ACP application (0.24 MPa for 10 s). After patterning, 2 mL cultured medium of fully supplemented VascuLife was added and changed every other day.

Immunofluorescence staining of angiogenic sprouts and quantification

Prior to staining, patterned HUVENCs within the fibrin hydrogels were fixed in zinc-buffered formalin (Z-Fix, Anatech, Battle Creek, MI). After 10 min, the fixative was removed, and the samples were washed 2 times with PBS. Endothelial cell-specific lectin Ulex Europaeus Agglutinin I (UEA-I, Vector Laboratories, Burlingame, CA) was utilized to stain the HUVEC. A staining solution consisting of 1% BSA, 20 µg/mL rhodamine-labeled UEA-I, and 10 nM DAPI in PBS was incubated with a cell-embedded fibrin hydrogel sample and left for 45 min at room temperature. Samples were then washed with PBS 2–4 times prior to imaging. An optical microscope (Olympus IX81, Olympus) was used to take single fluorescent images of endothelial networks.

ImageJ (Fiji distribution, version 1.5.3; NIH, Bethesda, MD) was utilized to merge fluorescent and bright-field images. The Angiogenesis Tube Formation module in Metamorph Premier imaging software (https://www.moleculardevices.com/products/cellular-imaging-systems/acquisition-and-analysis-software/metamorph-microscopy, version 7.8.6.0, Molecular Devices, Sunnyvale, CA) was used to quantify the area of each fibrin hydrogel occupied by endothelial tubules as a metric of microvascular network coverage[68]. UEA-I images were converted to grayscale 8-bit images for alignment analysis of the angiogenic sprouts. ImageJ, supported by the Oval Profile plugin (https://imagej.net/ij/plugins/oval-profile.html), was used for 2D FFT analysis, and the 2D FFT intensity at a given angle was defined as alignment[47]. The rescaled alignment was subtracted 1 from the output that was normalized by the minimum value.

For quantification, five images per construct were taken over a 50 μm depth (10 slices at 5 μm thick) at 4X magnification. Slices were superimposed using maximum intensity z-projection, and the length of sprouts was quantified using the Angiogenesis Tube Formation module in Metamorph Premier (Molecular Devices).

Patterning of hPSCs to form Neural tube-like structures (NTLS) using ACP

Colonies of hPSCs in tissue culture plates were dissociated using Accutase (Sigma-Aldrich) at 37 °C for 8 min before being suspended in DMEM/F12 (GIBCO) as single cells. Cells were then centrifuged and re-suspended in 30% Geltrex-mTeSR containing 10 µM Y27632 (Tocris), a ROCK inhibitor that prevents dissociation-induced apoptosis of hPSCs, at a concentration of 10×10^6 cells/mL. For patterning in a glass-bottom cell culture dish, 100 µL hPSC suspension in 30% Geltrex at 4 °C and brought to room temperature was introduced into the dish, and ACP with a slit structure was applied for 10–30 s.

To generate NTLS using ACP, patterning of hPSCs was performed in a microfluidic device fabricated based on a previous design[50]. Briefly, the microfluidic device was fabricated with five parallel channels defined and separated by arrays of microposts on a glass slide, including a central channel flanked by two parallel channels on each side. Each post had a diameter of 200 μm and the posts were spaced at a periodic interval of 150 μm. The inner sets of posts served to confine the injected sol-cell suspension within the central channel by surface tension. After solidification, liquid Geltrex was introduced and confined in the channels outside the central channel by the other sets of posts. The medium within the center of each channel via surface tension during loading, while still permitting the diffusion of neurodevelopmental factors across adjacent channels.

For patterning in a microfluidic device[50], 10 µL hPSC suspension with 30% Geltrex (at 4 °C) was brought to room temperature and introduced into the central channel through the loading port on the microfluidic device (day 0). The microfluidic device was placed on the 3D-printed slits structure for 10–30 s ACP application. Then the device with the cells was incubated at 37 °C for 10 min to complete Geltrex solidification. Subsequently, geltrex was introduced into the adjacent channels and incubated for an additional 10 min. The two medium reservoirs of the central channel are then immediately filled with fresh mTeSR medium containing 10 µM Y27632.

After patterning and on day 1, the culture medium in the left and right reservoirs of the central channel was switched to a neural

induction medium (NIM) comprising the basal medium and dual SMAD inhibitors (DSi; TGF-β inhibitor SB431542, 10 μM, STEMCELL Technologies; BMP4 inhibitor LDN193189, 200 nM, STEMCELL Technologies) to induce neural differentiation.

To generate rostral-caudal (R-C) patterned NTLS, CHIR99021 (CHIR, 3 μM, STEMCELL Technologies), FGF8 (200 ng mL-1, PEPROTECH), and retinoic acid (RA, 500 nM, STEMCELL Technologies) were supplemented into NIM in the right reservoir of the central channel from day 2 to day 5. Culture medium in the left and right medium reservoirs was switched back to fresh NIM from day 5 to day 7, or from day 5 to day 12. The medium was replenished daily.

For D-V patterning of NTLS, CHIR (3 μM), FGF8 (200 ng mL^{-1}), and RA (500 nM) were supplemented in NIM in both channels at day 2 and day 3. From day 4 to day 7, the culture medium in the left channel was changed to new basal medium with BMP4 (25 ng ml^{-1}, R&D Systems), and the right channel was changed to basal medium supplemented with RA (500 nM) and SAG (500 nM, StemCell Technologies). All reservoirs were switched to fresh basal medium for day 8 and day 9.

EdU assay of NTLS

For Edu assays, 600 μL of 10 μM EdU working solution prepared using the Click-iT™ Plus EdU Cell Proliferation Kit for Imaging (Alexa Fluor™ 488 dye; Invitrogen™) was added to each microfluidic device and incubated for 1 h at 37 °C. The staining procedure followed the manufacturer's instructions, except that the incubation times of subsequent steps were adjusted to accommodate 3D tissues. Samples were fixed with 4% paraformaldehyde (PFA) at room temperature for 5 h. The microfluidic device was then carefully peeled off and lifted to allow reagent access to the previously gel-embedded tissue region. Cells were permeabilized with 0.5% Triton X-100 overnight at 4 °C. Samples were subsequently incubated with the Click-iT® Plus reaction cocktail for 3 h at room temperature, followed by Hoechst/DAPI nuclear staining for 3 h at room temperature.

Antibodies

All primary antibodies used in this study are commercially available and have been validated for the species and application (immunofluorescence/immunocytochemistry) used here by the respective manufacturers; validation statements, antibody profiles and citing literature are available on the manufacturers' websites via the catalogue numbers and RRIDs given in Table 2. All primary and secondary antibodies used for immunofluorescence in this study, together with their supplier, catalogue number, RRID, clone (where applicable), and working dilution, are listed in Table 2.

Primary antibodies were diluted in phosphate-buffered saline (PBS) containing 4% (v/v) donkey serum (Sigma-Aldrich) and applied overnight at 4 °C. Secondary antibodies were diluted in the same buffer and applied overnight at 4 °C. Cell nuclei were counterstained with 4′,6-diamidino-2-phenylindole (DAPI; Thermo Fisher Scientific) applied together with the secondary antibodies. Antibody specificity in our hands was further supported by the expected subcellular localization of each marker (for example, nuclear localization of OCT4, NANOG, SOX2, GATA3, ISL1, TFAP2A, TFAP2C, SOX17 and the HOX proteins; apical/junctional localization of ZO-1 and EZRIN; membrane-associated localization of β-catenin) and by the absence of signal in secondary-antibody-only controls.

Immunofluorescence imaging of YAP

Fluorescence staining was performed on samples patterned with μCP and ACP after one day of culture, using an anti-YAP primary antibody (clone D8H1X, Cell Signaling Technology, cat. no. 14074, 1:200) and DAPI (4′,6-diamidino-2-phenylindole; Thermo Fisher Scientific); full antibody details are given in Table 2. Confocal microscopy was used to capture images of the samples, obtaining confocal images for both the DAPI and YAP channels. Image analysis was carried out using ImageJ. The nuclear area of cells was determined from the DAPI images, while the YAP fluorescence images indicated the distribution area of YAP within the cells. Cells are classified as YAP distributed either in the nucleus or outside the nucleus. The percentage of cells with nucleus YAP was calculated by the cell number with YAP among the total number of cells. The results showed that cells patterned by ACP exhibited a higher nuclear YAP percentage compared to cells on μCP patterns, indicating that YAP in ACP-patterned cells was more concentrated in the nucleus, whereas in μCP-patterned cells, YAP was more broadly distributed in the cytoplasm.

Immunofluorescence staining of NTLS

After overnight incubation with 4% donkey serum (Sigma-Aldrich) to block non-specific binding, samples were incubated overnight at 4 °C with primary antibodies against ZO-1, OCT4, SOX2, OTX2 (FB/MB marker), HOXB1 (HB marker), HOXB4 (HB/SC marker), HOXC9 (SC marker), HOXC10 (SC marker), and, for dorsoventral patterning, PAX3, SOX10 and OLIG2, followed by overnight incubation with the corresponding Alexa Fluor-conjugated donkey secondary antibodies. All primary antibodies were used at 1:200, and all secondary antibodies at 1:400; suppliers, catalogue numbers, and RRIDs are listed in Table 2. Cell nuclei were stained with DAPI (Thermo Fisher Scientific).

NTLS were imaged using an Olympus IX81 inverted microscope equipped with a spinning-disk confocal (Yookogawa CSU-X1), solid-state lasers (Solamere Technology) controlled by a National Instruments DAQmx, and an iXON3 EMCCD camera (Andor Technology). An array of partially overlapping images (50% overlap) was taken by MetaMorph software (Molecular Devices) to cover the entire NTLS area. Images were stitched using the ImageJ plugin MIST. The intensity heatmaps of lineage markers were generated using a custom MATLAB script. Briefly, DAPI images were used to generate a binary mask delineating the NTLS area. Fluorescence intensity values for each lineage marker within the masked regions were summed pixel-wise across multiple experiments and subsequently normalized to the maximum cumulative intensity, producing normalized heatmaps representing aggregate spatial marker distributions

Patterning of hPSCs to form epiblast-like structures using ACP

Before patterning hPSCs using ACP in a glass bottom (MATTEK, 35 mm dish, No. 1.5 coverslip, 14 mm glass diameter), the dish was treated with UV-ozone for 7 min (Ozone cleaner; Jelight).

For patterning hPSCs on an ECM bed, 15 μl of undiluted Geltrex™ was evenly spread on the glass on ice and stored in a 4 °C fridge for up to 3 hours before patterning. Before the use for the ACP experiment, the dish was placed in the incubator 37 °C for 30 min.

To form hPSC cysts, colonies of hPSCs in tissue culture plates were dissociated using Accutase (Sigma-Aldrich) at 37 °C for 8 min before being suspended in DMEM/F12 (GIBCO) as single cells. The cells were then centrifuged and resuspended in mTeSR containing 10 μM Y27632 (Tocris) at a concentration of 5×10^5 cells/mL. Next, 100 μL of the hPSC suspension was added to the central well of a glass-bottom dish, or to an ECM bed on day 0. The dish was then placed on a 3D-printed slit structure for ACP application for 10–25 s. The slit structure was then rotated 90-degree for a second ACP application for 10 – 45 s. The dish was left undisturbed for 5 min to allow cell attachment before being transferred to an incubator at 37 °C. On day 1 (24 h afterwards), the culture medium was replenished with fresh mTeSR1 without Y27632 for continuous culture. From day 2, a 3D culture protocol was applied, with the culture medium changed to mTeSR with 4% (v:v) Geltrex™ supplemented. Thereafter, mTeSR medium was replenished daily.

Brillouin imaging and quantification

Brillouin microscopy is based on the principle of spontaneous Brillouin scattering[62], which is an interaction between incident laser light and

Table 2 | Antibodies used for immunofluorescence

Target / antigen	Supplier	Catalogue no.	RRID	Host / clone	Dilution
Primary antibodies					
OCT4	Santa Cruz Biotechnology	sc-5279	AB_628051	Mouse monoclonal (C-10)	1:200
NANOG	Cell Signaling Technology	4903	AB_10559205	Rabbit monoclonal (D73G4)	1:200
SOX2	Cell Signaling Technology	3579	AB_2195767	Rabbit monoclonal (D6D9)	1:200
SOX10	R&D Systems	AF2864	AB_442208	Goat polyclonal	1:200
SOX17	R&D Systems	AF1924	AB_355060	Goat polyclonal	1:200
OTX2	R&D Systems	AF1979	AB_2157172	Goat polyclonal	1:200
HOXB1	R&D Systems	AF6318	AB_10972265	Sheep polyclonal	1:200
HOXB4	DSHB	I12 anti-Hoxb4	AB_2119288	Rat monoclonal (I12)	1:200
HOXC9	Abcam	ab50839	AB_880494	Mouse monoclonal	1:200
HOXC10	Abcam	ab153904	AB_2687827	Rabbit polyclonal	1:200
PAX3	DSHB	Pax3	AB_2315061	Mouse monoclonal (Pax3)	1:200
OLIG2	Proteintech	13999-1-AP	AB_2157541	Rabbit polyclonal	1:200
ZO-1	Thermo Fisher Scientific	33-9100	AB_2533147	Mouse monoclonal (ZO1-1A12)	1:200
EZRIN	Sigma-Aldrich	E8897	AB_476955	Mouse monoclonal (3C12)	1:200
Brachyury (T/TBXT)	Thermo Fisher Scientific	PA5-46984	AB_2610378	Goat polyclonal	1:200
YAP	Cell Signaling Technology	14074	AB_2650491	Rabbit monoclonal (D8H1X)	1:200
β-Catenin	Cell Signaling Technology	8480	AB_11127855	Rabbit monoclonal (D10A8)	1:200
GATA3	Cell Signaling Technology	5852	AB_10835690	Rabbit monoclonal (D13C9)	1:200
ISL1	DSHB	39.4D5	AB_2314683	Mouse monoclonal (39.4D5)	1:200
TFAP2A	Abcam	ab108311	AB_10861200	Rabbit monoclonal	1:200
TFAP2C	Santa Cruz Biotechnology	sc-8977	AB_2286995	Rabbit polyclonal	1:200
Phospho-SMAD1/SMAD5 (pSMAD1/5)	Thermo Fisher Scientific	700047	AB_2532276	Rabbit polyclonal	1:200
F-actin	Thermo Fisher Scientific	MA1-80729	AB_936561	Mouse monoclonal	1:200
Laminin	Sigma-Aldrich	L9393	AB_477163	Rabbit polyclonal	1:200
Secondary antibodies					
Donkey anti-rabbit IgG, Alexa Fluor 546	Thermo Fisher Scientific	A10040	AB_2534016	Donkey polyclonal	1:400
Donkey anti-mouse IgG, Alexa Fluor 488	Thermo Fisher Scientific	A-21202	AB_141607	Donkey polyclonal	1:400
Donkey anti-mouse IgG, Alexa Fluor 546	Thermo Fisher Scientific	A10036	AB_2534012	Donkey polyclonal	1:400
Donkey anti-goat IgG, Alexa Fluor 647	Thermo Fisher Scientific	A-21447	AB_2535864	Donkey polyclonal	1:400
Donkey anti-rat IgG, Alexa Fluor 488	Thermo Fisher Scientific	A-21208	AB_2535794	Donkey polyclonal	1:400
Donkey anti-sheep IgG, Alexa Fluor 647	Thermo Fisher Scientific	A-21448	AB_2535865	Donkey polyclonal	1:400
Other stains					
DAPI (nuclear counterstain)	Thermo Fisher Scientific	–	–	–	as per manufacturer
Rhodamine-labeled UEA-I lectin	Vector Laboratories	–	–	–	20 μg mL^{-1}

thermally induced acoustic phonons inherent to the material. This interaction results in scattered light that has a frequency shift ω, given by $\omega = \frac{2n}{\lambda}\sqrt{\frac{M'}{\rho}}\sin\left(\frac{\theta}{2}\right)$, where n is the refractive index of the material, λ is the laser wavelength, M' is the longitudinal modulus, ρ is mass density, and θ is the scattering angle. With the assumption that the ratio of refractive index and density (i.e., $n/\sqrt{\rho}$) is approximately constant in biological samples, Brillouin shift can be used to estimate the relative change of longitudinal modulus[69,70].

The Brillouin shift at each spatial location of the sample was acquired using a self-built confocal Brillouin microscope[71]. Briefly, a 660 nm laser was used as the light source, and the laser beam was focused onto the sample through an objective lens (40×/0.6, Olympus), achieving a spot size of approximately 0.7 μm laterally and 2.5 μm axially. The same objective lens was used to collect the backscattered ($\theta = 180°$) Brillouin signal. The Brillouin spectra of the scattered light were analyzed using a two-stage virtually imaged phased array (VIPA) spectrometer. Samples were maintained in an on-stage incubator (Okolab) at 37 °C and 5% CO_2 throughout the experiments. The laser power at the sample was set at 20 mW, with an acquisition speed at 25 ms per pixel. Brillouin images were acquired via scanning at a step size of 1 μm in the lateral direction and 2 μm in the axial direction.

Images of the Brillouin shift of hPSC-derived cysts in this experiment were obtained from the sagittal plane and two transverse planes of the cysts, and averages of the Brillouin shifts were computed for each specified plane. The averaged shifts in the sagittal plane were only computed using the Brillouin-shift data in the lower half of the sagittal plane (near the basal interface with the substrate) of all cysts, because the Brillouin shifts were degraded in the top half due to decreased signal at increased imaging depth.

At increased imaging depths, refractive index inhomogeneity and optical scattering within the sample perturb the propagation trajectory of the incident laser beam in the Brillouin microscope. These effects distort the focal volume and change the scattering geometry, such that the effective scattering angle deviates from the 180° backscattering condition. Consequently, the measured Brillouin shift is reduced, introducing depth-dependent artifacts. In experiments, signal intensity was used as a practical criterion to determine the artifact-free depth range for quantitative analysis.

Table 3 | qRT-PCR primer sequences

Gene	Forward (5′ to 3′)	Reverse (5′ to 3′)
GAPDH	CTCTGCTCCTCCTGTTCGAC	TTAAAAGCAGCCCTGGTGAC
BMP2	ACTACCAGAAACGAGTGGGAA	GCATCTGTTCTCGGAAAACCT
BMP4	TCCACAGCACTGGTCTTGAG	GGGATGTTCTCCAGATGTTCTT
BMP6	AGCGACACCACAAAGAGTTCA	GCTGATGCTCCTGTAAGACTTGA
BMP7	TCGGCACCCATGTTCATGC	GAGGAAATGGCTATCTTGCAGG

Immunostaining of epiblast-like structures

After overnight incubation with 4% donkey serum (Sigma-Aldrich) to block non-specific binding, samples were incubated overnight at 4 °C with primary antibodies against OCT4, NANOG, SOX2, EZRIN, ZO-1, β-catenin, F-actin, laminin, GATA3, ISL1, TFAP2A, phospho-SMAD1/5, TFAP2C, SOX17 and Brachyury, as indicated in the corresponding figures, followed by overnight incubation with the corresponding Alexa Fluor-conjugated donkey secondary antibodies. All primary antibodies were used at 1:200, and all secondary antibodies at 1:400; suppliers, catalogue numbers, RRIDs, and clones are listed in Table 2. Cell nuclei were counterstained with 4′,6-diamidino-2-phenylindole (DAPI; Thermo Fisher Scientific) applied together with the secondary antibodies. Confocal images were acquired using an Olympus 1 × 81 fluorescence microscope with a CSU-X1 spinning-disc unit (YOKOGAWA) or a Nikon A1 laser scanning confocal microscope. Measurements were performed using the Measurement tool in ImageJ (NIH). DAPI staining was cross-checked with other antibody staining regions.

qRT-PCR of hPSC-derived cysts

Cells were collected from cysts on day 4 or 6. Reverse transcription of isolated total RNA was performed using the iScriptTM cDNA synthesis Kit (Bio-Rad). qRT-PCR analysis was performed by an investigator who was blinded to group allocation using the Quantitect Sybr Green MasterMix (QIAGEN) on a CFX ConnectTM Real-Time System (Bio-Rad) for 40 cycles. Human GAPDH was used as an internal control for quantifying relative gene expression by using the 2−ΔCt method. The primer sequences used for this study are listed in Table 3.

Statistical Analysis

Statistical analyses were performed using MATLAB R2025a and RStudio (R 4.4.1). Data are presented as mean ± s.d. unless otherwise indicated; the measure of centre and the error shown are defined in each figure legend. Sample size (n), defined as the number of independent biological replicates (independent experiments, individual cysts, lumens, or fields of view, as specified per experiment), is stated in the corresponding figure legend for every quantified panel. Comparisons between two groups were performed using an unpaired two-tailed Student's t-test. Comparisons among three or more groups were performed using analysis of variance (ANOVA) followed by multiple-comparison correction. Differences were considered statistically significant at $P < 0.05$, and exact P values are reported in the figure legends and in the accompanying Source Data file. All experiments were repeated at least three times independently on separately prepared cell-culture batches with consistent results; the number of independent repeats for each representative micrograph is stated in its figure legend. Biological replicates refer to independent experiments performed on separately seeded and patterned samples; technical and biological replicates were not conflated.

Reporting summary

Further information on research design is available in the Nature Portfolio Reporting Summary linked to this article.

Data availability

The source data underlying all quantitative results in the main and Supplementary Figs. are included as a Source Data file and have been deposited in the Zenodo database under (https://doi.org/10.5281/zenodo.21265507). The COMSOL model files used for the acoustic simulations are available in the same Zenodo deposition. The raw confocal, bright-field, infrared and Brillouin imaging datasets generated in this study are available upon request from the corresponding authors; these datasets are not deposited in full because of their size, and no restrictions apply to their availability. Source data are provided with this paper.

References

1. Schrom, E. C. et al. Spatial Patterning Analysis of Cellular Ensembles (SPACE) finds complex spatial organization at the cell and tissue levels. *Proc. Natl. Acad. Sci. USA* **122**, e2412146122 (2025).
2. Fu, J., Warmflash, A. & Lutolf, M. P. Stem-cell-based embryo models for fundamental research and translation. *Nat. Mater.* **20**, 132–144 (2021).
3. Shao, Y. & Fu, J. Engineering multiscale structural orders for high-fidelity embryoids and organoids. *Cell Stem Cell* **29**, 722–743 (2022).
4. Abel, A. & Sozen, B. Shifting early embryology paradigms: applications of stem cell-based embryo models in bioengineering. *Curr. Opin. Genet Dev.* **81**, 102069 (2023).
5. Perl, A., Reinhoudt, D. N. & Huskens, J. Microcontact printing: limitations and achievements. *Adv. Mater.* **21**, 2257–2268 (2009).
6. Hu, S., Chen, T. H., Zhao, Y., Wang, Z. & Lam, R. H. W. Protein-substrate adhesion in microcontact printing regulates cell behavior. *Langmuir* **34**, 1750–1759 (2018).
7. Vijayavenkataraman, S., Yan, W. C., Lu, W. F., Wang, C. H. & Fuh, J. Y. H. 3D bioprinting of tissues and organs for regenerative medicine. *Adv. Drug Deliv. Rev.* **132**, 296–332 (2018).
8. Ji, S. & Guvendiren, M. Recent Advances in Bioink Design for 3D Bioprinting of Tissues and Organs. *Front Bioeng. Biotechnol.* **5**, 23 (2017).
9. Murphy, S. V. & Atala, A. 3D bioprinting of tissues and organs. *Nat. Biotechnol.* **32**, 773–785 (2014).
10. Zhang, B. et al. 3D bioprinting: an emerging technology full of opportunities and challenges. *Bio-Des. Manuf.* **1**, 2–13 (2018).
11. Mota, C., Camarero-Espinosa, S., Baker, M. B., Wieringa, P. & Moroni, L. Bioprinting: from tissue and organ development to in vitro models. *Chem. Rev.* **120**, 10547–10607 (2020).
12. Thomson, J. A. et al. Embryonic stem cell lines derived from human blastocysts. *Science* **282**, 1145–1147 (1998).
13. Takahashi, K. & Yamanaka, S. Induction of pluripotent stem cells from mouse embryonic and adult fibroblast cultures by defined factors. *Cell* **126**, 663–676 (2006).
14. Nakano, T. et al. Self-formation of optic cups and storable stratified neural retina from human ESCs. *Cell Stem Cell* **10**, 771–785 (2012).
15. Lancaster, M. A. et al. Cerebral organoids model human brain development and microcephaly. *Nature* **501**, 373–379 (2013).
16. Poh, Y. C. et al. Generation of organized germ layers from a single mouse embryonic stem cell. *Nat. Commun.* **5**, 4000 (2014).

17. Warmflash, A., Sorre, B., Etoc, F., Siggia, E. D. & Brivanlou, A. H. A method to recapitulate early embryonic spatial patterning in human embryonic stem cells. *Nat. Methods* **11**, 847–854 (2014).
18. Ma, Z. et al. Self-organizing human cardiac microchambers mediated by geometric confinement. *Nat. Commun.* **6**, 7413 (2015).
19. Shao, Y. et al. A pluripotent stem cell-based model for post-implantation human amniotic sac development. *Nat. Commun.* **8**, 208 (2017).
20. Tewary, M. et al. A stepwise model of reaction-diffusion and positional-information governs self-organized human peri-gastrulation-like patterning. *Development* **144**, 4298–4312 (2017).
21. Clevers, H. Modeling development and disease with organoids. *Cell* **165**, 1586–1597 (2016).
22. Huch, M., Knoblich, J. A., Lutolf, M. P. & Martinez-Arias, A. The hope and the hype of organoid research. *Development* **144**, 938–941 (2017).
23. Lancaster, M. A. & Knoblich, J. A. Organogenesis in a dish: modeling development and disease using organoid technologies. *Science* **345**, 1247125 (2014).
24. Rossant, J. & Tam, P. P. L. Opportunities and challenges with stem cell-based embryo models. *Stem Cell Rep.* **16**, 1031–1038 (2021).
25. Sasai, Y. Cytosystems dynamics in self-organization of tissue architecture. *Nature* **493**, 318–326 (2013).
26. Shamir, E. R. & Ewald, A. J. Three-dimensional organotypic culture: experimental models of mammalian biology and disease. *Nat. Rev. Mol. Cell Biol.* **15**, 647–664 (2014).
27. Simunovic, M. & Brivanlou, A. H. Embryoids, organoids and gastruloids: new approaches to understanding embryogenesis. *Development* **144**, 976–985 (2017).
28. Turner, D. A., Baillie-Johnson, P. & Martinez Arias, A. Organoids and the genetically encoded self-assembly of embryonic stem cells. *Bioessays* **38**, 181–191 (2016).
29. Wu, J. & Fu, J. Toward developing human organs via embryo models and chimeras. *Cell* **187**, 3194–3219 (2024).
30. Shao, Y. et al. Self-organized amniogenesis by human pluripotent stem cells in a biomimetic implantation-like niche. *Nat. Mater.* **16**, 419–425 (2017).
31. Zheng, Y. et al. Dorsal-ventral patterned neural cyst from human pluripotent stem cells in a neurogenic niche. *Sci. Adv.* **5**, eaax5933 (2019).
32. Xue, X., Liu, Y. & Fu, J. Bioengineering embryo models. *Nat. Rev. Bioeng.* **3**, 11–29 (2025).
33. Sloan, S. A., Andersen, J., Pasca, A. M., Birey, F. & Pasca, S. P. Generation and assembly of human brain region-specific three-dimensional cultures. *Nat. Protoc.* **13**, 2062–2085 (2018).
34. Bazou, D., Kuznetsova, L. A. & Coakley, W. T. Physical enviroment of 2-D animal cell aggregates formed in a short pathlength ultrasound standing wave trap. *Ultrasound Med. Biol.* **31**, 423–430 (2005).
35. Garvin, K. A., Dalecki, D., Yousefhussien, M., Helguera, M. & Hocking, D. C. Spatial patterning of endothelial cells and vascular network formation using ultrasound standing wave fields. *J. Acoust. Soc. Am.* **134**, 1483–1490 (2013).
36. Garvin, K. A., Dalecki, D. & Hocking, D. C. Vascularization of three-dimensional collagen hydrogels using ultrasound standing wave fields. *Ultrasound Med. Biol.* **37**, 1853–1864 (2011).
37. Comeau, E. S., Hocking, D. C. & Dalecki, D. Ultrasound patterning technologies for studying vascular morphogenesis in 3D. *J. Cell Sci.* **130**, 232–242 (2017).
38. Bouyer, C. et al. A bio-acoustic levitational (BAL) assembly method for engineering of multilayered, 3d brain-like constructs, using human embryonic stem cell derived neuro-progenitors. *Adv. Mater.* **28**, 161–167 (2016).
39. Armstrong, J. P. K. et al. Engineering anisotropic muscle tissue using acoustic cell patterning. *Adv. Mater.* **30**, e1802649 (2018).
40. Armstrong, J. P. K. et al. Spatiotemporal quantification of acoustic cell patterning using Voronoi tessellation. *Lab Chip* **19**, 562–573 (2019).
41. Kang, B. et al. High-resolution acoustophoretic 3D cell patterning to construct functional collateral cylindroids for ischemia therapy. *Nat. Commun.* **9**, 5402 (2018).
42. Armstrong, J. P. K. et al. Tissue engineering cartilage with deep zone cytoarchitecture by high-resolution acoustic cell patterning. *Adv. Health. Mater.* **11**, e2200481 (2022).
43. Gesellchen, F., Bernassau, A. L., Dejardin, T., Cumming, D. R. & Riehle, M. O. Cell patterning with a heptagon acoustic tweezer-application in neurite guidance. *Lab Chip* **14**, 2266–2275 (2014).
44. Settnes, M. & Bruus, H. Forces acting on a small particle in an acoustical field in a viscous fluid. *Phys. Rev. E Stat. Nonlin. Soft Matter Phys.* **85**, 016327 (2012).
45. Zhang, L. & Marston, P. L. Acoustic radiation force expressed using complex phase shifts and momentum-transfer cross sections. *J. Acoust. Soc. Am.* **140**, EL178 (2016).
46. Newman, A. C., Nakatsu, M. N., Chou, W., Gershon, P. D. & Hughes, C. C. The requirement for fibroblasts in angiogenesis: fibroblast-derived matrix proteins are essential for endothelial cell lumen formation. *Mol. Biol. Cell* **22**, 3791–3800 (2011).
47. Ayres, C. E. et al. Measuring fiber alignment in electrospun scaffolds: a user's guide to the 2D fast Fourier transform approach. *J. Biomater. Sci. Polym. Ed.* **19**, 603–621 (2008).
48. Piard, C. et al. 3D printed HUVECs/MSCs cocultures impact cellular interactions and angiogenesis depending on cell-cell distance. *Biomaterials* **222**, 119423 (2019).
49. Skrzypek, K. et al. An important step towards a prevascularized islet macroencapsulation device-effect of micropatterned membranes on development of endothelial cell network. *J. Mater. Sci. Mater. Med.* **29**, 91 (2018).
50. Xue, X. et al. A patterned human neural tube model using microfluidic gradients. *Nature* **628**, 391–399 (2024).
51. Du, Z. W. et al. Generation and expansion of highly pure motor neuron progenitors from human pluripotent stem cells. *Nat. Commun.* **6**, 6626 (2015).
52. Gouti, M. et al. In vitro generation of neuromesodermal progenitors reveals distinct roles for Wnt signalling in the specification of spinal cord and paraxial mesoderm identity. *PLoS Biol.* **12**, e1001937 (2014).
53. Crossley, P. H., Martinez, S. & Martin, G. R. Midbrain development induced by FGF8 in the chick embryo. *Nature* **380**, 66–68 (1996).
54. Liu, A. & Joyner, A. L. Early anterior/posterior patterning of the midbrain and cerebellum. *Annu Rev. Neurosci.* **24**, 869–896 (2001).
55. Niederreither, K. & Dolle, P. Retinoic acid in development: towards an integrated view. *Nat. Rev. Genet.* **9**, 541–553 (2008).
56. Mancini, F. E. et al. Effect of a retinoic acid analogue on BMP-driven pluripotent stem cell chondrogenesis. *Sci. Rep.* **14**, 2696 (2024).
57. Deschamps, J. & Duboule, D. Embryonic timing, axial stem cells, chromatin dynamics, and the Hox clock. *Genes Dev.* **31**, 1406–1416 (2017).
58. Le Dreau, G. & Marti, E. Dorsal-ventral patterning of the neural tube: a tale of three signals. *Dev. Neurobiol.* **72**, 1471–1481 (2012).
59. Liem, K. F. Jr., Tremml, G., Roelink, H. & Jessell, T. M. Dorsal differentiation of neural plate cells induced by BMP-mediated signals from epidermal ectoderm. *Cell* **82**, 969–979 (1995).
60. Novitch, B. G., Wichterle, H., Jessell, T. M. & Sockanathan, S. A requirement for retinoic acid-mediated transcriptional activation in ventral neural patterning and motor neuron specification. *Neuron* **40**, 81–95 (2003).
61. Dessaud, E., McMahon, A. P. & Briscoe, J. Pattern formation in the vertebrate neural tube: a sonic hedgehog morphogen-regulated transcriptional network. *Development* **135**, 2489–2503 (2008).

62. Kabakova, I. et al. Brillouin microscopy. *Nat. Rev. Methods Prim.* **4**, 8 (2024).
63. Blaeser, A. et al. Controlling shear stress in 3D bioprinting is a key factor to balance printing resolution and stem cell integrity. *Adv. Health. Mater.* **5**, 326–333 (2016).
64. Li, F. et al. Phononic-crystal-based acoustic sieve for tunable manipulations of particles by a highly localized radiation force. *Phys. Rev. Appl.* **1**, https://doi.org/10.1103/PhysRevApplied.1.051001 (2014).
65. Cai, F. et al. Acoustic trapping of particle by a periodically structured stiff plate. *Appl. Phys. Lett.* **99**, https://doi.org/10.1063/1.3670267 (2011).
66. He, Z. et al. Acoustic transmission enhancement through a periodically structured stiff plate without any opening. *Phys. Rev. Lett.* **105**, 074301 (2010).
67. Marzo, A. et al. Holographic acoustic elements for manipulation of levitated objects. *Nat. Commun.* **6**, 8661 (2015).
68. Friend, N. E. et al. Injectable pre-cultured tissue modules catalyze the formation of extensive functional microvasculature in vivo. *Sci. Rep.* **10**, 15562 (2020).
69. Scarcelli, G. et al. Noncontact three-dimensional mapping of intracellular hydro-mechanical properties by Brillouin microscopy. *Nat. methods* **12**, 1132–1134 (2015).
70. Zhang, J. et al. Nuclear mechanics within intact cells is regulated by cytoskeletal network and internal nanostructures. *Small* **16**, 1907688 (2020).
71. Zhang, J. & Scarcelli, G. Mapping mechanical properties of biological materials via an add-on Brillouin module to confocal microscopes. *Nat. Protoc.* **16**, 1251–1275 (2021).

Author contributions

Z.X., W.L., and X.X. performed experiments. Z.X. and W. L. analyzed data and generated figures. W.L. performed COMSOL simulation and constructed experimental setup. J.P.S. guided vessel formation study. N.G.S. helped with vessel formation experiments and data analysis. W.L., C.S., and J.Z. performed Brillouin microscopy and obtained measurements. R.Y., S.S., and J.B. participated in PCR experiments and analysis. J.F. and C.X.D. led the experiments, data analysis, and writing of the manuscript.

Funding

This research was supported by the Michigan-Cambridge Collaboration Initiative, a University of Michigan Mid-career Biosciences Faculty Achievement Recognition Award, the National Science Foundation of the United States (CMMI 2517721, CMMI 2325361, PFI 2213845, and EFMA 2422149), and the US National Institutes of Health (R21 NS127983, R01 GM143297, and R01 NS129850).

Competing interests

The authors declare no competing interests.

Additional information

Supplementary information The online version contains supplementary material available at https://doi.org/10.1038/s41467-026-76976-5.

Correspondence and requests for materials should be addressed to Jianping Fu or Cheri X. Deng.

Peer review information *Nature Communications* thanks Ryuji Yokokawa, who co-reviewed with Kazuya Fujimoto and Ma ChengAbdel Rahman Abdel Fattah, and the other, anonymous, reviewer(s) for their contribution to the peer review of this work. A peer review file is available.

Reprints and permissions information is available at http://www.nature.com/reprints

Publisher's note Springer Nature remains neutral with regard to jurisdictional claims in published maps and institutional affiliations.

Open Access This article is licensed under a Creative Commons Attribution-NonCommercial-NoDerivatives 4.0 International License, which permits any non-commercial use, sharing, distribution and reproduction in any medium or format, as long as you give appropriate credit to the original author(s) and the source, provide a link to the Creative Commons licence, and indicate if you modified the licensed material. You do not have permission under this licence to share adapted material derived from this article or parts of it. The images or other third party material in this article are included in the article's Creative Commons licence, unless indicated otherwise in a credit line to the material. If material is not included in the article's Creative Commons licence and your intended use is not permitted by statutory regulation or exceeds the permitted use, you will need to obtain permission directly from the copyright holder. To view a copy of this licence, visit http://creativecommons.org/licenses/by-nc-nd/4.0/.

© The Author(s) 2026